Nanoscale

Accepted Manuscript

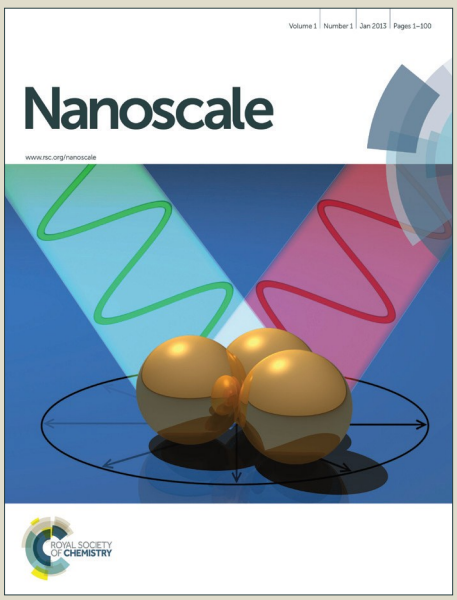

ROYAL SOCIETY OF CHEMISTRY

www.rsc.org/nanoscale

Study of the nucleation and growth of antibiotic labeled Au NPs and blue luminescent Au_8 quantum clusters for Hg^{2+} ion sensing, cellular imaging and antibacterial applications

Puneet Khandelwal[1,2], Dheeraj K. Singh[1,2], Subha Sadhu[1,2], Pankaj Poddar*[1,2,3]

[1]Physical & Material Chemistry Division, CSIR-National Chemical Laboratory, Pune – 411008, India, [2]Academy of Scientific and Innovative Research, Anusandhan Bhawan, 2 Rafi Marg, New Delhi-110 001, [3]Center of Excellence on Surface Science, CSIR-National Chemical Laboratory, Pune – 411008, India

*Corresponding author:

E-mail: p.poddar@ncl.res.in

Physical and Material Chemistry Division,

CSIR-National Chemical Laboratory,

Dr. Homi Bhabha Road

Pune- 411008, India

Phone: +91-20-2590-2580 (Office)

Fax: +91-20-2590-2636

Abstract

Herein, we report a detailed experimental study supported by DFT calculations to understand the mechanism behind the synthesis of cefradine (CFD- an antibiotic) labeled gold nanoparticles (Au NPs) by employing CFD as both mild reducing and capping agent. The analysis of the effect of growth conditions reveals that higher concentration of $HAuCl_4$ results into the formation of increasing fraction of anisotropic structures, higher temperature leads to the formation of quasi-spherical particles in comparison to anisotropic ones, and larger pH leads to the formation of much smaller particles. The cyclic voltammetry (CV) results show that when the pH of the reaction medium increases from 4 to 6, the reduction potential of CFD increases which leads to the synthesis of nanoparticles (in pH 4 reaction) to quantum clusters (in pH 6 reaction). The MALDI-TOF mass spectrometric results of supernatant of pH 6 reaction indicate the formation of $[Au_8(CFD)_2S_6]$ QCs which show the fluorescence at ca. 432 nm with a Stokes shift of ca. 95 nm. The blue luminescence from Au_8 QCs was applied for sensing of Hg^{2+} ions on the basis of an aggregation-induced fluorescence quenching mechanism and offers good selectivity and a high sensitivity with a limit of detection ca. 2 nM which is lower than the detection requirement of 10 nM by the U.S. EPA and 30 nM by WHO for drinking water. We have also applied the sensing probe to detect the Hg^{2+} ions in the bacterial samples. Further, we have investigated the antibacterial property of as-synthesized Au NPs using MIC, growth curve and cell survival assay. The results show that Au NPs could reduce the cell survival very efficiently rather than the cell growth in comparison to the antibiotic itself. The scanning electron microscopic study shows the degradation and blabbing of bacterial cell wall upon exposure with Au NPs which was further supported by fluorescence microscopic results. These Au NPs did not show the reactive oxygen species generation. We believe that the bacterial cytotoxicity is due to the direct contact of the Au NPs with bacterial cells.

Introduction

It is fascinating as well as challenging to explore the effect of reaction conditions (monomer concentration, temperature and pH of the reaction) on the nucleation and growth mechanism behind the formation of nanocrystallites in the solution phase; starting from monomers (atoms/molecules/ions). The role of reduction potential of reducing agents and relative binding affinities of capping agents to different lattice facets, in the formation and stabilization of larger (tens of nm or larger) and sub-nm metal clusters (which are otherwise not stable), is also interesting. These fundamental studies are non-trivial even for much simpler model system such as the formation gold nanoparticles (Au NPs) by the reduction of Au^{3+} ions.[1–3] It is already well researched that among the metal NPs, Au NPs are more fascinating because of their low toxicity,[4–7] size and shape dependent optical properties at the nanoscale[5,8–14] which make them interesting for applications in many fields such as biosensor,[9,15–17] drug delivery,[18–21] and catalysis.[22] Interestingly, these properties become even more fascinating when the size decreases to an extent, when it becomes comparable to the Fermi wavelength of an electron (ca. 0.5 nm for Au).[23,24] The particles in this small size regime called quantum clusters (QCs) which are made up of few atoms to few tens of atoms and exhibit size-dependent fluorescence.[25–28] The fluorescence of these Au QCs generally follows a simple relation $E_{Fermi}/n^{1/3}$, known as Jellium model.[29] The electronic properties of Au NPs as well as Au QCs heavily depend on the surface modification with suitable functional molecules, which provide additional tunability and functionality.[11,30–33]

In a typical noble metal NP synthesis, the use of strong reducing agents (e.g. $NaBH_4$, citric acid etc.) result into the formation of highly monodispersed particles. While using the strong reducing agents, the monomer concentration instantaneously drops below the saturation limit and that stops further nucleation events, therefore, it is difficult to experimentally probe and follow the growth events (*in situ*) using the conventional photon

correlation techniques based on scattering as the nucleation and growth of Au NPs using stronger reducing agents usually ends in a fraction of second. In contrast, the antibiotic mediated synthesis method gives an edge over the conventional methods as recently reported by our group.[8,10] Due to the fact that beta lactam antibiotic molecules are weaker reducing agents, (1) we get polydispersed particles, as fresh nuclei keep forming while the existing particles grow further (2) we observe the formation of stable quantum clusters by tuning the reaction parameters, and (3) due to the slow kinetics, it is easy to do follow the reaction pathways to some extent by doing a time dependent study of the particle evolution using light scattering, absorption spectroscopy or electron microscopy techiques.[8–10,34] Recently, our group used an in situ, real-time, static/dynamic light scattering and absorption spectroscopy measurements in combination with electron microscopy imaging, to track the time evolution of seeds and noticed the simultaneous growth of two different populations of Au NPs (quite different in sizes). We have noticed that the smaller particles (diameter < 2 nm) could grow and coexist simultaneously with larger particles (diameter > 40 nm) and the larger particles were the results of aggregation of smaller clusters to form isotropic/anisotropic nanocrystallites.[10] We also reported the effect of concentration of monomers and the reaction temperature on the nucleation and growth mechanism.[8] In another study, our group has also shown the synthesis of antibiotic (cefadroxil, CFX) labeled blue emissive Au QCs and their application in the sensing of Sn^{4+} ions.[9]

In the present study, we have used cefradine, as a model system, to study the nucleation and growth of antibiotic labeled Au NPs and blue luminescent Au_8 quantum clusters for Hg^{2+} ion sensing, cellular imaging and antibacterial applications. Cefradine is a β-lactam antibiotic, effective against a wide range of Gram-positive and a limited range of Gram-negative bacteria.[35] This is relatively resistant to β-lactamases[36] and has a tendency to interact with metal ions. In comparison to cefadroxil (CFX), cefradine (CFD) does not have –

OH group at the 4th position of phenyl ring. The use of antibiotic molecules as reducing and surface capping agent for the synthesis of Au NPs and blue luminescent Au QCs may add few key advantages. The luminescent nature of the Au QCs may be useful for imaging and sensing applications.[9,37] The capping of antibiotic onto the nanoparticles may synergistically enhance the antibacterial properties of these particles.[34,38–41] Therefore, first, the interaction of the luminescent Au QCs with various heavy and toxic metal ions is investigated for sensing applications. It is found that Au QCs can be used to sense as low as ca. 2 nM concentration of mercury ions in pH 7 buffer with high selectivity over various metal ions based on a mechanism involving particle aggregation-induced fluorescence quenching, possibly due to screening of charges of Au QCs after binding selectively with cations. Mercury is one of the serious environment pollutant and most hazardous heavy metal ion which ultimately accumulates in the human body via food chain and possesses the serious health issues related to immune, nervous and digestive systems and affects the lungs, kidneys, skin and eyes.[42] It also affects the development of the child in utero and early in life. The maximum permitted level of mercury in drinking water by WHO and the U.S. Environmental Protection Agency (EPA) has set at 30 and 10 nM, respectively.[43] In view of these facts, it is very essential to detect the presence of Hg^{2+} ions in environment at very low concentrations especially at nano-molar range. We have also demonstrated the use of the Hg^{2+} ion-sensing probe for detection of the Hg^{2+} ions in the bacterial cells.

The interaction of the metal ions and nanoparticles with biological entities is another very interesting issue for researchers. In an earlier investigation, while probing the effect of Co^{2+} ions on marine bacterium, our group observed that the bacterial cells exhibit co-operative, self-organized and structured colonies under the stress of Co^{2+} ions which triggers a redox process mediated by the biomolecules that results in to the formation of Co_3O_4 NPs and the microbial cells also undergo tremendous change in their nanomechanical behavior

such as cellular adhesion, elasticity, and plasticity as probed by in situ AFM investigation.[44] In contrast to the interaction of cells with ions, the study of interaction of stable nanoparticles with certain microbes also comes with novel results.[45–47] Recently, our group reported the novel process of biomilling where the large particles such as ZnO nanorods can be milled to much smaller quasi-spherical nanoparticles upon interaction with yeast *S. cerevisae*.[47] In present manuscript, the Au NPs are capped with antibiotic molecules so it becomes very interesting to study the fate of the antimicrobial activity of the antibiotic molecules in the proximity to the Au NPs surfaces. According to a recent report, there are very much conflicting results in the literature about the antibacterial activity of Au NPs.[48] Au NPs are generally considered as not bactericidal or weakly bactericidal. In view of these facts, we have performed detailed investigations for the antibacterial properties of CFD labeled Au NPs against *E. coli*, a Gram-negative rod shaped model bacterium to contribute towards the understanding about the antibacterial activity of antibiotic capped Au NPs.

Materials and Method

Materials

All the chemicals were of analytical grade and used as-received without any further purification, unless otherwise described. The reagents $HAuCl_4.3H_2O$ (≥ 49.0% Au basis), dibasic sodium phosphate (> 99%), monobasic sodium phosphate (> 99%), CH_3COOK (> 99%), sodium acetate (≥ 99 %), acetic acid (> 99.7%), $Ni(NO_3)_2.6H_2O$ and fluorescein diacetate (FDA) were purchased from Sigma Aldrich. Cefradine was purchased from Fluka and $(NH_4)_2Ce(NO_3)$ (99.9%), $Mg(NO_3)_2{\cdot}6H_2O$, $Al(NO_3)_3{\cdot}9H_2O$, $Zn(NO_3)_2.6H_2O$ (96 – 103%), $LiNO_3$, propidium iodide (PI) and 2′,7′-dichlorofluorescein (DCF) were purchased from Loba chemie. The reagents $Pb(NO_3)_2$, $Hg(NO_3)_2.H_2O$, $NaNO_3$, $Cu(NO_3)_2.3H_2O$, KNO_3, $Ba(NO_3)_2$ (> 99%), and $MgCl_2$ were purchased from Merck; and $Cr(NO_3)_3.9H_2O$ (98–101%),

$Cd(NO_3)_2.4H_2O$, $Cr(NO_3)_3.9H_2O$, $Fe(NO_3)_2.9H_2O$, KCl, and NaCl were purchased from Thomas baker. $AgNO_3$ was purchased from RFCL limited. $CaCl_2$ was purchased from BDH chemicals. Luria Bertani (LB) and agar powder were purchased from Himedia. All glassware were washed with aquaregia (HCl: HNO_3 = 3:1) carefully and rinsed with double distilled water before using them for synthesis.

Synthesis of CFD labeled Au NPs

The CFD labeled Au NPs were synthesized by the addition of CFD molecules in aqueous medium (final concentration of CFD molecules in the mixture was 5×10^{-4} M) in $HAuCl_4$ solution (final concentration in mixture was varied from 10^{-4} M to 10^{-3} M) followed by continuous stirring for 2 h at 27 ^{o}C. We have also studied the effect of varying the reaction temperature (10 ^{o}C to 50 ^{o}C) and pH (4 to 8) on Au NPs size and morphology in the presence of both CFD and $HAuCl_4$ at a final concentration of 5×10^{-4} M. In the synthesis of CFD labeled Au NPs, CFD itself provides the sequestration site for Au^{3+} ions and acts as both mild reducing and capping/stabilizing agent, without further use of any other reducing agents or templates.

Isolation of Au QCs

During the course of the reaction performed at pH 6, the simultaneous production of Au NPs and Au QCs in the reduction of $HAuCl_4$ with CFD occurred and the color of the solution changed from an original light-yellow to a final dark-brown. Probably, the Au QCs have been generated by the modulated reduction of $HAuCl_4$ by CFD at pH 6. Relatively larger particles were removed at the end of reaction through centrifugation at 15000 rpm for 15 min, providing a light-brown supernatant containing the Au QCs.

Effect of pH and ionic strength on the fluorescence of Au QCs

We have investigated the effect of pH on the fluorescence of Au QCs by varying the pH of the medium from pH 4, pH 7, and pH 10 using buffer solutions. The effect of ionic

strength of various salts like NaCl, KCl, $MgCl_2$, and $CaCl_2$ on the fluorescence of Au QCs was also investigated by addition of these salts in a concentration range from 0.01 M to 0.2 M. An aliquot of Au QCs suspension was added to pH 7 buffer containing various concentrations of NaCl/KCl/$MgCl_2$/$CaCl_2$ salts. The mixture was shaken vigorously and left for 5 min. The fluorescence emission spectra were then recorded at the excitation of 337 nm.

Fluorescence based detection of Hg^{2+} ions using fluorescent Au QCs

Herein, we have developed the fluorescence quenching based sensor for Hg^{2+} ions. We have investigated the effect of adding various metal ions (100 μM, all metal ions were taken as nitrate salts and the reaction pH were maintained at pH 7 using phosphate buffer) on the fluorescence of CFD labeled Au QCs. An aliquot of Au QCs suspension (10 μL) was added to 1 mL pH 7 buffer containing various concentrations of Hg^{2+} ions. The solution was mixed thoroughly and left to react at room temperature for 5 min. The fluorescence emission spectra were then recorded at the excitation of 337 nm.

Fluorescence microscopic imaging based detection of Hg^{2+} ions in bacterial cells using Au QCs as Hg^{2+} ion sensing probe

The *E. coli* cell suspension with $O.D._{600}$ (optical density measured at 600 nm) ca. 0.1 was treated with Au QCs at the final concentration of 20 μg/mL for 2 h. The Au QCs were first dialyzed with benzoylated dialysis tube with MWCO ca. 2 kDa to ensure the removal ionic impurities and unbound antibiotic molecules. We have also performed the MIC test of dialyzed Au QCs to ensure the concentration of Au QCs used should not be itself toxic to the bacterial cells. After 2 h incubation, the cells were pelleted-out by centrifugation at 10,000 g for 10 min at 4 ^{o}C, washed twice with PBS buffer and re-suspended in PBS buffer. An aliquot from of the bacterial cells were taken from the above cells suspended in PBS buffer and incubated for 5 min with Hg^{2+} ions, followed by washing with PBS buffer. Finally, the cells

with and without Hg^{2+} treatments were drop-casted onto the two separate glass slides and covered with coverslip by nail polish for fluorescence microscopic examination.

Antibacterial study of Au NPs

The Au NPs synthesized at pH values of 4, 5 and 6 were dialyzed against double-distilled water for 24 h and named as pH 4 Au NPs, pH 5 Au NPs, and pH 6 Au NPs, respectively. The water was replaced and changed at least two times during the dialysis process, before using the dialyzed Au NPs for bacterial cytotoxicity determination to ensure the removal of ionic impurities and unbound antibiotic**.** For this purpose, *E. coli* culture (NCIM 2064) was sourced from National Collection of Industrial Microorganisms (NCIM), CSIR-National Chemical Laboratory, Pune, India and was stored as agar slant at 4 ^{o}C (not exceeding 2 weeks). For every experiment, a loop-full of bacterial culture was taken and inoculated in fresh LB medium and grown at standard culture condition of 37 ^{o}C at 180 rpm shaking speed.

Minimum inhibitory concentration (MIC) determination

The MIC value corresponds to the concentration of compound at which the bacterial growth is inhibited by as much as 90% compared with the control. We determined the MIC value using microbroth dilution method. For this purpose, overnight grown culture of *E. coli* cells was added into fresh LB medium to give a concentration of $O.D._{600}$ ca. 0.1. This culture was equally distributed in 9 different culture tubes. Eight culture tubes were added with various amounts of Au NPs (pH4/ pH5/ pH6, on the basis of antibiotic concentration used for reaction and assumed that all the antibiotic molecules consumed at the time of Au NPs synthesis)/ CFD in such a way that final concentration will be 64, 32, 16, 8, 4, 2, 1, 0.5 μg/mL. The culture tubes without NPs and without inoculum were used as positive and negative control, respectively. The cultures were then grown at 37 ^{o}C, 180 rpm for 18 h and the optical density at 600 nm was measured. The experiment was done in triplicates.

Reduction in cell growth

For this purpose, overnight grown culture of *E. coli* cells were used as seed culture. This seed culture was added into fresh LB medium to give a concentration of $O.D._{600}$ ca. 0.1. This culture was equally distributed in five different culture tubes. Then, the CFD labeled Au NPs (synthesized at pH 4, pH 5, pH 6), and CFD were added into four different culture tubes at the final concentration of 64 μg/mL. The culture without nanoparticles was used as positive control. The cultures were then grown at 37 ^{o}C, 180 rpm for 18 h. The culture was withdrawn from each culture tube at every 2 h and $O.D._{600}$ was measured. The experiment was done in triplicates.

Cell survival assay

The cell survival assay was performed using colony count method. For this, the *E. coli* cell suspension (in PBS) with $O.D._{600}$ ca. 0.1 was incubated with Au NPs (synthesized at pH 4, 5 and 6) and CFD at the final concentration of 64 μg/mL for 24 h at 180 rpm and 37 ^{o}C temperature. The cells suspended in PBS buffer were used as control. 100 μl aliquots were taken out from each sample at 0 h and 24 h; and diluted to 10^{-3} dilution, plated on the petri plate and incubated at 37 ^{o}C for 18 h to visualize the colonies. The digital images of the plates were captured. The experiment was performed in triplicates.

Sample preparation for SEM imaging

The *E. coli* cell suspension with $O.D._{600}$ ca. 0.1 was treated with Au NPs (synthesized at pH 4, 5 and 6) and CFD at the final concentration 64 μg/mL for 4 h. Following that, the cells were pelleted-out by centrifugation at 10,000 g for 10 min at 4 ^{o}C, washed twice with PBS buffer and resuspended in 2% gluteraldehyde solution and incubated for 20 min. Then, these cells were again washed twice with PBS buffer (pH=7.4, 0.01M) by centrifugation at 10,000 g for 10 min at 4 °C and were drop-casted on to the Si wafer and coated with gold for SEM imaging.

Sample preparation for fluorescence microscopy

The *E. coli* cell suspension with $O.D._{600}$ ca. 0.1 was treated with Au NPs (synthesized at pH 4, 5 and 6) and CFD at the final concentration 64 μg/mL for 24 h. The *E. coli* cell suspension in PBS buffer was treated as control. After 24 h incubation, the cells were pelleted-out by centrifugation at 10,000 g for 10 min at 4 ^{o}C, washed twice with PBS buffer and resuspended in PBS buffer. The propidium iodide (PI) dye was added at the final concentration of ca. 10 μM, incubated for 20 min in dark and washed with PBS buffer. Finally, the cells were drop-casted onto the glass slide and covered with coverslip by nail polish.

ROS determination

The *E. coli* suspension with $O.D._{600}$ ca. 0.1 was treated Au NPs (concentration 64 μg/mL) for 6 h. After incubation period of 6 h, the cells were pelletized by centrifugation at 10,000 g for 10 min at 4 °C, washed twice with PBS buffer and re-suspended in PBS buffer. DCF dye was added to above bacterial suspension at a final concentration of 5 μM and incubated for 1 h, at mild shaking. DCF dye is a non-fluorescent dye and gets converted to fluorescent dye in the presence of ROS; it determines the presence of intracellular ROS. The presence of fluorescent DCF dye was measured at an emission wavelength of 525 nm upon exciting the sample at an excitation wavelength 488 nm. The ROS concentration is considered directly proportional to the fluorescence intensity of the DCF dye. The experiment was performed in triplicates.

Characterization techniques

Absorbance spectra were recorded using a Jasco UV-vis-NIR dual beam spectrometer (Model V570) operated at a resolution of 2 nm. Excitation and emission spectra were recorded using a Cary Eclipse photoluminescence spectrophotometer from Varian equipped with Xenon flash lamp. Time-resolved fluorescence measurements were performed on a time

correlated single photon counting (TCSPC) spectrometer (Horiba Jobin Yvon IBH, UK). The detailed description of the instrument can be found elsewhere.[49] TEM images of CFD labeled Au NPs were recorded using Tecnai G-2 T20 transmission electron microscope (TEM) working at accelerating voltage of 200 kV. HR-TEM measurements on the CFD labeled Au QCs were performed using a Tecnai F30 HR-TEM from FEI Inc., equipped with field emission source operating at 300 kV with S-TWIN objective lens and Cs value of 1.2 mm. The point resolution of the microscope was 0.24 nm. The sample was drop-casted on a carbon coated copper grid and air-dried for imaging. The cyclic voltammetry measurements were performed using CH Instruments Potentiostats. The CFD solution concentration was kept constant to 1mM and the lithium perchlorate (100 mM) was used as an electrolyte. The counter, working and reference electrodes were Pt foil, Pt wire and Ag/AgCl electrodes. Powder XRD patterns were recorded using a PANalytical X'Pert PRO instrument and the iron-filtered Cu-Kα radiation (λ = 1.54 Å) in the 2θ range of 10–80° with a step size of 0.02°on drop-coated samples on glass substrate. FTIR spectra were obtained using a Perkin-Elmer Spectrum One instrument. The spectrometer operated in the % transmission mode at a resolution of 2 cm^{-1}. Raman spectroscopy measurements were recorded at room temperature on an HR 800 Raman spectrophotometer (Jobin Yvon, Horiba, France) using monochromatic radiation emitted by a He-Ne laser (633 nm), operating at 20 mW. The experiment was repeated several times to verify the consistency of the recorded spectra. The samples for the Raman studies were prepared simply by drop-casting the liquid onto the glass slide. X-ray photoelectron spectroscopy (XPS) analysis was done on a VG Micro Tech ESCA 3000 instrument at a pressure of < $1x10^{-9}$ Torr with the overall resolution of 1 eV. The spectra were recorded with unmonochromatic Mg Kα radiation at pass energy of 50 eV and an electron take off angle of 60^{o}. The sample was drop casted on a clean Si wafer, and air-dried for analysis. Mass spectra were collected by using MALDI TOF/TOF Instrument (AB SCIEX

TOF/TOF™ 5800 System). As-synthesized Au QCs suspension was mixed with DHB (in methanol) in 1:1 ratio by volume. Then, 0.5 μL of this solution was deposited on a MALDI target plate and air-dried. The plate was inserted into the instrument and irradiated by a Nd: YAG laser. Scanning electron microscopic study has been performed using FEI Quanta 200 environmental SEM to evaluate the morphological changes in the bacterial cells in presence and absence of Au NPs. A PALS Zeta Potential Analyzer Ver 3.54 (Brookhaven Instrument Corps.) was used to determine the electrophoretic mobilities. Mobilities were converted to zeta potential (ζ) using the Smolochowski model. The fluorescence microscopic images were taken by Carl Zeiss inverted fluorescence microscope model Axio Observer.Z1.

DFT computational method

All the theoretical calculations were performed using Gaussian 09 programming package.[50] The geometrical optimization of CFD and its various possible conjugations with Au^{3+} ions were calculated in gas phase as well as bulk solvation using Density Functional Theory (DFT) with B3LYP hybrid functional, which is found to be very useful in predicting molecular properties.[51–54] In the present study, Lanl2dz basis set[55] was employed for the heavy Au atom as recent reports indicated its good performance[56–58] and 6-311++g(d, p) basis set for C, H, N, O and S atoms containing molecules in all the calculations. Since experimentally all the synthesis were performed in aqueous environment, so having the condition quite close to the experiment, polarizable continuum model (PCM)[59] was also taken into account for the bulk solvent effects in all the calculation.

Results and discussion

Study of growth kinetics of CFD labeled NPs

In order to visualize the effect of variation in the $HAuCl_4$/CFD concentration, temperature and pH on the morphology of the particles, we performed a detailed UV-vis-NIR spectroscopic and TEM study as follows:

Effect of $HAuCl_4$/CFD concentration on the morphology of the Au NPs

As indicated earlier, CFD labeled Au NPs have been synthesized by the addition of CFD aqueous solution (final concentration in the mixture was 5×10^{-4} M) in $HAuCl_4$ aqueous solution (final concentration in the mixture was varied from 10^{-4} M to 10^{-3} M) and incubated for 2 h at 25 ^{o}C followed by UV-vis-NIR spectroscopic analysis (figure 1a). When $HAuCl_4$ concentration in the mixture was 10^{-4} M, a single peak was observed in the visible region ca. 550 nm that corresponds to the transverse component of surface plasmon resonance (TSPR). The TSPR peak indicates the formation of isotropic NPs in the suspension. The broadness of the TSPR peak and long tail part extending into NIR region also indicate the presence of polydispersed particles. When the final concentration of $HAuCl_4$ was increased to 3×10^{-4} M, the NIR absorption get enhanced along with a relative increase in the TSPR peak and an appearance of shoulder at ca. 720 nm due to longitudinal component of surface plasmon resonance (LSPR). This feature indicates the presence of anisotropic Au NPs (along with isotropic NPs) with an increasing fraction.[8] Interestingly, when the final concentration of $HAuCl_4$ in the mixture was further increased to 8×10^{-4} M and 10^{-3} M, the LSPR peak (and overall absorption in the NIR region) became more prominent with continuous shift towards higher wavelength at ca. 870 nm and 1100 nm, respectively, (figure 1a) which is symptomatic of an increment in the edge length of anisotropic nanoparticles.[60]

The influence of $HAuCl_4$/CFD concentration on the morphology of as-synthesized CFD labeled Au NPs has also been studied by TEM and the results were consistent with UV-vis spectroscopic results. The TEM images in the figures 1b, c, and d correspond to the formation of CFD labeled Au NPs when the final concentration of $HAuCl_4$ in the mixture

was 10^{-4} M, 5×10^{-4} M, and 10^{-3} M, respectively (for CFD concentration 5×10^{-4} M). For the $HAuCl_4$ concentration of 10^{-4} M, a clear observation of bimodal distribution of isotropic (quasi-spherical) NPs with an average size ca. 13 nm was noticed. When the $HAuCl_4$ concentration was increased to 5×10^{-4} M, a small population of triangular shaped Au NPs (edge length ca. 40 nm), with a large population of quasi-spherical NPs formed. Upon increase in the concentration to 10^{-3} M, a larger population of triangular shaped particles (edge length ca. 150 nm) was synthesized. As we discussed earlier, the polydispersity of the Au NPs is due to the fact that antibiotic molecules are weak reducing agents in comparison to citric acid and $NaBH_4$ etc, which leads to relatively slow growth kinetics that, in turn, allows the low energy surface facets to expose and bind with chloride ions. For each Au^{3+} ion, there would be four times increment in the Cl^- ions in the solution. Retardation of growth along the <111> direction due to preferential chemisorption of Cl^- ions on the (111) lattice planes could be the conceivable reason behind the formation of anisotropic nanostructures.[61] Further, to study the effect of variation of temperature and pH, on the synthesis of Au NPs by CFD, equimolar (5×10^{-4} M) concentration of both CFD and $HAuCl_4$ in final solution was used as a default concentration. The results are discussed in the sections below.

Effect of reaction temperature on the morphology of the Au NPs

The effect of temperature on the synthesis of CFD labeled Au NPs was also studied by mixing the pre-thermalized (at the specific temperature mentioned here) solutions of CFD and $HAuCl_4$ (final concentration of both in the mixture was 5×10^{-4} M) at a temperature range from 10 ^oC to 50 ^oC and corresponding UV-vis-NIR spectra have been shown in figure 2a. When the reaction temperature was 10 ^oC, in addition to the TSPR peak, we found a broad absorption even beyond 1200 nm, which indicated the growth of relatively large anisotropic nanostructures. However, for the growth at higher temperatures (ca. 20 ^oC and 30 ^oC), the NIR absorption got reduced and the relative peak intensity of TSPR got enhanced.

The TSPR peak also showed blue-shift, indicating the reduction in the particle size.[60] Interestingly, when the reaction was carried out at further higher temperatures (40 ^{o}C and 50 ^{o}C), the LSPR peak disappeared suggesting the formation of isotropic Au NPs only (figure 2a).

Figures 2 b and c compare the TEM images of CFD labeled Au NPs synthesized at 50 ^{o}C and 10 ^{o}C, respectively. At 50 ^{o}C, the growth of nearly isotropic NPs was observed with an average size ca. 15 nm (figure 2b). At 10 ^{o}C, a sharp change in the particle morphology can be easily noticed with a larger fraction of triangular shaped NPs (edge length ca. 120 nm). These results were consistent with UV-vis-NIR absorption spectroscopy. The synthesis of gold nanotriangles is a relatively slow process and can occur at low temperature where the rate of reduction of metal ions become low and possibly facilitates the oriented growth of nuclei and thus promotes the formation of anisotropic NPs.[62–64] Increase in the temperature of the reaction results in an increase in the rate of reduction of gold ions which leads to an enhanced nucleation rate and the consumption of most of the chloroaurate ions in the formation of nuclei, results in the stalled secondary reduction process on the surface of the preformed nuclei.[60] As a result, a much higher population of spherical NPs in comparison with triangular ones was obtained which shows that a simple variation in the reaction temperature enables the synthesis and tailoring of the size of the triangular NPs.

Effect of reaction pH on the morphology of the Au NPs

The pH effect on the synthesis of Au NPs has also been investigated by mixing the CFD and $HAuCl_4$ solutions at final concentration of 5×10^{-4} M from pH range 4 to 8. The drastic changes have been observed, when the reaction was performed at different pH environments. A comparison of the UV-vis-NIR spectra indicated that, as the pH of reaction was increased from 4 to 5, the TSPR peak is blue-shifted from ca. 566 nm to ca. 532 nm and

the color of the suspension changes from purple to intense red, indicating a decrease in the average size of quasi-spherical Au NPs. Interestingly, at pH 6, the color of suspension completely changed to brown and SPR peak almost disappeared with just a broad absorption peak visible at ca. 360 nm, indicating the dominant synthesis of gold particles with size below 2 nm[25] (in addition to some big particles). At pH 7 and 8, the solution became colorless and showed the maximum absorption at ca. 357 nm and ca. 351 nm, respectively. This might be the sign of the presence of gold - antibiotic complexes in the solution (figure 3a).[65,66]

To validate the absorption spectroscopy results, TEM analysis of the CFD labeled Au NPs synthesized at pH 4, 5 and 6 was performed and presented in figures 3c, d and e. TEM images corresponding to pH 7 and 8 have not been shown (as we were unable to find Au NPs in these samples). Figure 3c shows the presence of both isotropic and anisotropic population of Au NPs with an average size ca. 20 nm. At pH 5, a larger fraction of the NPs seems to be isotropic in nature with an average size ca. 12 nm. In agreement with the results of UV-vis-NIR absorption, at pH 6, an average particle size was decreased to ca. 1 nm, along with relatively smaller population of bigger NPs with an average size ca. 6 nm. We have also measured the hydrodynamic diameter of the as synthesized particles at different pH to further have an idea about particle distribution in the suspension and the results were well correlated with the UV-vis and TEM results. The analysis of pH 4 suspension (Figure S1) shows that a large population of particles from 19 - 50 nm with a small population of particles or their aggregates with a size around 200 nm was present. Some aggregates were very large even a size around 5 micron. Whereas at pH 5, a large population of ca. 9 - 13 nm particles with a small population of big nanoparticles and/or their small aggregates (ca. 50 nm) were observed (Figure S2). Figure S3 shows the presence of a large population of ca. 3 - 4 nm particles with a small population of big nanoparticles and/or their small aggregates (ca. 18 nm). Therefore, it can be concluded that the suspension synthesized at pH 4 was highly unstable (starts to

settle down within 1.5 h) compared to the particle suspension synthesized at pH 5 and pH 6 (did not settle after storage for even 2 days at room temperature, figure S4). Therefore, pH of the reaction medium is an extremely crucial factor in the synthesis of Au NPs. It is anticipated that the reduction from Au^{3+} to Au^{0} for synthesis of nanoparticles, would depend on the reduction potential of CFD molecules which itself depends on the pH of the reaction medium. It is evident from the cyclic voltammetry study that upon increase in the pH from 4 to 7, the reduction potential of CFD has increased from ca. 0.45 V, 0.53 V, 0.58 V to 0.63 V, respectively (figure 3b). Therefore, in summary, the ability of synthesis of Au NPs using CFD molecule depends on the pH of reaction mixture to the great extant and will decrease upon increase in the pH from 4 to 7.

The change in the crystalline structure of the synthesized CFD labeled Au NPs at different concentration of $HAuCl_4$, temperature and pH of the reaction (where the final concentration of both the constituents (CFD and $HAuCl_4$) was 5×10^{-4} M and reaction temperature was 27 ^{o}C), was studied through PXRD and presented in Figure S5a, b and c, respectively. The XRD pattern revealed the relative dominance of (111) plane when the Au NPs synthesized at higher $HAuCl_4$ concentrations, decrease in the temperature and decrease in pH of the reaction indicating the increase in the synthesis of anisotropic nanostructures. Moreover, FTIR, Raman and XPS studies have been performed to analyze the functional group(s) responsible for binding of CFD to Au NPs surface. FTIR and Raman spectroscopic results (figures S6 and S7, respectively) indicate the possible involvement of $-NH_2$ and >C=O groups in the binding of CFD to Au NPs surface. Whereas XPS results in figure S8 indicate that amine and carbonyl group of (probably, β-lactam ring) CFD molecule simultaneously plays important role in binding to Au NPs surface. We also used DFT calculations to investigate the interactions between Au^{3+} ions and CFD molecule where the

special emphasis was put on the analysis of geometrical configurations, electronic structures and electron transfers between CFD and Au^{3+} ions complexes during the interaction.

Calculation of optimized geometries of CFD and its conjugation with Au^{3+} ions using density functional theory

The initial geometries of Au^{3+} ions and CFD complexes were optimized by placing Au^{3+} ions near the possible active sites of CFD molecule. The active sites of CFD molecules are sulfur, carbonyl and amine groups and their corresponding numbering (from 1 to 5) was presented in figures 4 a to f. Due to the electron rich moieties in these groups, the tendency to form the anchoring bonds with Au^{3+} ions in the complexes increases. Further, Au^{3+} can also play the role as a proton acceptor and form nonconventional hydrogen bonds with hydroxide (Au···H–O) as shown in figure 4b. These two factors could also be responsible for the stability of the complexes of CFD with Au^{3+} ions. The interaction between CFD and Au^{3+} ions is either monodentate or bidentate, where, in the latter case, it usually involves non-conventional hydrogen bonding.

For this study, we started our calculations by first checking the binding of Au^{3+} ions with sulfur group of CFD (figure 4a i.e. CFD + 1Au_1). Our calculations yield Au-S anchoring bonds with bond length of 2.34 Å, which is very close to the sum of the covalent radii 2.36 Å of S (1.02 Å) and Au (1.34 Å).[67] The result is in good agreement with a previously calculated value of 2.45 Å.[68] Thus, one may expect a stronger covalent contribution to the sulfur bonding. The reduction in charge of Au^{3+} to $Au^{-0.015}$ was also taking place upon formation of Au-S anchoring bonds as shown in Table S1 and figure 4 a. Further, we checked the possibility of binding of Au^{3+} ions with carbonyl group of CFD molecule. There are three possibilities of adding the Au^{3+} ions with carbonyl group of CFD molecule that is denoted by CFD + 1Au_2, CFD + 1Au_3 and CFD + 1Au_4 and displayed in figure 4 b, c, and d, respectively. In the CFD + 1Au_2 and CFD + 1Au_3 complex, the Au-O bond

lengths were 2.15 and 2.17 Å and charge reduction down to $Au^{+0.628}$ and $Au^{+0.580}$, respectively. The input geometry of CFD+1Au_4 complex got completely changed to CFD+1Au_3 structure after optimization (see figure 4d to 4e). These results clearly suggest that among the three Au-O bond formations, the CFD+1Au_3, which belongs to β-lactam ring, shows the stronger interactions and reduction property.

The interaction of the Au^{3+} ions with amine group of CFD (see figure 4f i.e. CFD+1Au_5) was also calculated which yields Au-N bond length of 2.02 Å which is very close to the sum of the covalent radii of nitrogen (0.75 Å) and Au (1.35 Å)[68] indicating a stronger bond. The interaction of two CFD molecules with one Au^{3+} ion was also considered and the same trend (discussed above) of bond formation and reduction in Au^{3+} ions were obtained and shown in figures S10 a, b, and c, respectively.

Apart from studying interaction of one Au^{3+} ion with CFD, we also calculated the interaction of two and three Au^{3+} ions with CFD molecule, simultaneously, especially at sulfur and amine groups as shown in figures 5a to 5c. However, earlier DFT calculations have shown that the DFT results obtained by taking a single metal atom are sufficient to describe the experimental results.[69–71] In the case of CFD + 2Au_1 and CFD + 3Au_1 complex (figure 5a and b), the Au-S anchoring bonds are calculated to be 2.39 Å and 2.37 Å and the corresponding average Au-Au distances are found to be 3.06 Å and 3.30 Å, respectively. In the case of CFD + 3Au_5 complex (figure 5c), the bidentate interaction was taking place where the Au-N and Au-O anchoring bonds were calculated to be 2.07 and 2.08 Å, respectively and the average Au-Au distance was found to be 3.51 Å. The average charge reduction of Au^{3+} ions in different complexes were also presented in Table S1, which clearly indicates the reduction of Au^{3+} to Au^{0} state. Thus, on the basis of strong Au-S, Au-N and Au-O bond, calculated binding energies and reduction in charges of Au^{3+} ions, one may easily

conclude that the sulfur plays a dominant role in reduction / binding to Au NPs surfaces, however, the amine and carbonyl groups (β-lactam ring) also play role in stabilizing the NPs.

The electrostatic potential surface has been mapped and shown in figures 5d, and 5e for CFD and its complex with Au^{3+} ions *i.e.* CFD+ 1 Au_1, respectively (for detailed see supporting information). Such surfaces depict the size, shape, charge density, and site of chemical reactivity of the molecules. The different values of the electrostatic potential at the surface are represented by different colors; red represents regions of most negative electrostatic potential, blue represents regions of most positive electrostatic potential, and green represents regions of zero potential. Potential increases in the order red < orange < yellow < green < blue. In figures 5d, and 5e, the electrostatic potential at different points on the electron density isosurface is shown by coloring the isosurface with contours. In the case of CFD, the O atom of β-lactam ring shows most negative electrostatic potential (red color). However, in the case of CFD+1Au_1 complex the significant amount of charge was transferred as shown in figure 5e.

The time dependent Density Functional Theory (TD-DFT) excited state calculations of the lowest singlet-singlet and singlet-triplet excitations of CFD + 1Au_1 complexes performed in water using PCM method. The calculated values of corresponding most probable electronic transitions having larger vertical excitation and oscillator strength were presented in figure S12. The TD - DFT calculation of CFD + 1Au_1 complex in aqueous environment gives rise to the most prominent absorption bands at 511 nm with oscillator strength (f = 0.778) due to HOMO → LUMO + 1 transitions. In HOMO orbital of CFD + 1Au_1 system, the electron densities are mainly concentrated on the β-lactam ring moiety; while in LUMO + 1 orbital's the electron densities were shifted towards the Au (see figure S12). Our TD - DFT calculations clearly indicate the evidence of electron transfer from CFD

to the Au center and essentially indicate that Au^{3+} ions are reduced to ca. Au^0 as a consequence of complexation.

UV-vis spectroscopic and photoluminescence study of CFD labeled Au QCs

As mentioned earlier, the gold particle suspension synthesized at pH 6, was centrifuged at 15,000 rpm for 10 min to assure the absence of big nanoparticles in the brown colored supernatant. UV-vis spectrum of supernatant shows a continuous absorption in the UV range starting from ca. 470 nm as shown in figure $6a_2$ (green curve), in addition, the complete absence of SPR absorption peak at ca. 520 nm, confirms the presence of Au QCs with the size < 2 nm. It is important to mention that the UV-vis spectrum of Au QCs was quite different than the UV-vis spectrum of CFD aqueous solution, with a broad absorption peak at ca. 350 nm in Au QCs spectrum (compare curves (a_1) and (a_2) in figure 6a) which may be due to the ligand to metal ion charge transfer in CFD-Au ion complexes.[65,66]

Photoluminescence properties of Au QCs have also studied. Usually, the emission peak position of fluorescent Au QCs depends on the size of the Au QCs core. According to the spherical Jellium model, Au QCs with larger core size emit at longer wavelengths [e.g., UV (Au_5), blue (Au_8), green (Au_{13}), and red (Au_{25}) emission].[72,73] Here, the Au QCs suspension exhibits the blue luminescence with an excitation and emission maxima at ca. 337 nm and ca. 432 nm (figure $6a_3$, a_4), respectively, with Stokes shift of ca. 95 nm and quantum efficiency ca. 0.9%. This blue emission wavelength is close to the reported values for Au_8 QCs blue emission at λ_{em} = 450 nm from PAMAM[25] and BSA[74] encapsulated Au_8 QCs, λ_{em} = 455 nm from lysozyme type VI stabilized Au_8 QCs[75] and λ_{em} = 465 nm from Au_8 QCs[76] synthesized by etching of mercaptosuccinic acid capped Au NPs, which shows that the CFD labelled Au clusters were Au_8 QCs. Although, the fluorescence of Au QCs was less intense, but, it is slightly red shifted by around 4 nm with respect to the fluorescence of CFD alone (figure S13), and more intense than the CFD-Au NPs and pH 6 reaction suspension which

support the synthesis of Au QCs. To differentiate the Au QCs component from CFD fluorescence, the fluorescence lifetime decay study has performed on both samples and presented in the next section.

The effect of pH and salt concentration on the photoluminescence of Au QCs has also studies, and presented in figure S14 and S15, respectively. Upon increase in the pH from 4 to 7, the fluorescence of Au QCs has not changed but upon further increases in the pH to 10 leads to the enhancement of the fluorescence of Au QCs almost around two times. However, upon addition of various concentrations (10mM to 200 mM) of salts (NaCl, KCl, $MgCl_2$, and $CaCl_2$) did not affect the fluorescence of Au QCs meaningfully.

Time resolved fluorescence study

The time resolved fluorescence measurements of CFD aqueous solution and CFD labeled Au_8 QCs have been performed and compared in figure 6b. The fluorescence decay time analysis for both CFD aqueous solution and CFD labeled Au_8 QCs reveals a tri-exponential decay profile. The lifetime components for CFD aqueous solution were 0.94 ns (26.4%), 3.44 ns (67%) and 0.12 ns (6.6%) while for CFD labeled Au_8 QCs, the values were 1.21 ns (6.7%), 4.82 ns (0.8%) and 0.097 ns (92.5%). The average decay time for CFD alone was 2.56 ns whereas this value has been decreased to 0.2 ns for CFD labeled Au_8 QCs (Table 1). From the above data, it is clear that the lifetime of Au_8 QCs is markedly different from CFD aqueous solution alone. Generally, it has been observed that Au QCs exhibit a large component of a few tens of picoseconds and several small components of nanosecond[77] which were consistent with lifetime decay results for CFD labeled Au_8 QCs.

HR-TEM and MALDI-TOF mass spectroscopic study of CFD labeled Au QCs

The HR-TEM results also support the formation of Au QCs (figures 6c and inset) with the size ca. 0.5 nm (the corresponding population distribution histogram is presented in figure S16). Figure S17 presents mass spectrum of CFD, which shows substantial difference in

comparison with Au QCs mass spectrum. The figure 6d shows the positive ion linear mode mass spectrum for as-synthesized Au QCs, using low laser power to suppress the fragmentation. Interestingly, the mass spectrum contains very limited peaks with only one major peak that can be easily distinguished from other peaks. The figure 6d shows one major peak in the mass spectrum at the position of 2466.6 Da (this value is very close to the reported value ca. 2256.4 Da for the mass of Au_8 cluster)[78] assigned to $[Au_8(CFD)_2S_6]$ clusters (following Yang *et al.* peak assignment for gold clusters stabilized with penicillamine,[79] see Table S2 in supporting information).

Application of CFD labeled Au_8 QCs as **fluorescence probe for the detection of Hg^{2+} ions in solution**

The supernatant (isolated CFD labeled Au_8 QCs) was directly used as a highly sensitive and selective fluorescent "turn-off" sensor for Hg^{2+} ions without further modification. For this purpose, at first, the effect of the addition of various bivalent, trivalent and tetravalent (Hg^{2+}, Cd^{2+}, Pb^{2+}, Ce^{4+}, Ni^{2+}, Cr^{3+}, Ag^{+}, Li^{+}, Mg^{2+}, Al^{3+}, K^{+}, Ba^{2+}, Zn^{2+}, Cu^{2+}, Na^{+} and Fe^{3+}) metal ions (200 μM) on the fluorescence of CFD labeled Au_8 QCs was studied. The figure 7 a shows relative fluorescence (I_0/I) of CFD labeled Au_8 QCs in the presence of various metal ions. It can be seen from figure 7a that the fluorescence intensity of Au_8 QCs shows a substantial decrease for Hg^{2+} ions only and was nearly unaffected by other metal ions. The fluorescence intensity of CFD labeled Au QCs decreased linearly ($R^2 = 0.93$) over the Hg^{2+} ions concentration range of 10–100,000 nM and can be seen from dose response graph plotted in the inset of figure 7a. The fitted linear data could be expressed as

$$I_0/I = 0.67 + 0.2\,[Hg^{2+}]\ (R^2 = 0.93) \qquad (1)$$

The limit of detection (LOD) for Hg^{2+} ions was ca. 2 nM; the slope was 0.2 nM^{-1}. The fluorescence of CFD labeled Au QCs was effectively quenched by Hg^{2+} ions and showed approximately three-fold fluorescence quenching at 100 μM concentration of Hg^{2+} ions

(figure 7b). The fluorescence quenching in the presence of Hg^{2+} ions was attributed to the Au_8 QCs aggregation, which might be induced by CFD and Hg^{2+} ion complexation. Figures 7b inset shows the TEM images of Au_8 QCs before and after the Hg^{2+} ions treatment, respectively. The TEM images confirm the aggregation of Au_8 QCs.

Application of Au_8 QCs as a sensing probe to detect the Hg^{2+} ions in the bacterial cells

For this purpose, the overnight grown *E. coli* cells were washed, diluted in PBS buffer and incubated with Au_8 QCs for 2 h at 37 ^oC over a constant shaking speed of 180 rpm. Then, the cells were washed and spotted on glass slide for fluorescence microscope examination. The blue fluorescent bacterial cells were visualized under the fluorescence microscope showing the capability of Au_8 QCs to image the bacterial cells (Figure 8a, b). Addition of 10 μM mercury to the bacterial cells leads to a sharp decrease in the fluorescence of the cells which supports the application of the as-synthesized Au_8 QCs for the sensing of Hg^{2+} ions in biological samples (figure 8c, d).

Study of antibacterial activity of Au NPs

Minimum inhibitory concentration (MIC) determination

In order to investigate the antibacterial properties of Au NPs (synthesized at pH 4, pH 5 and pH 6) and CFD, the MIC test via the micro-broth dilution method, was performed. The MIC value for CFD was found ca. 8 μg/mL whereas for Au NPs, it was > 64 μg/mL (figure S18). The possible reason behind these results may be the negative charge present on the CFD labeled Au NPs (ca. -30 mV), which hinders the Au NPs to efficiently interact with negatively charged bacterial cells, especially in LB growth medium.[80]

Reduction in cell growth

To further investigate the effect of Au NPs on the growth of bacterial cells, the bacterial cells were treated with 64 μg/mL of Au NPs and growth of bacterial cells was observed over a period of 18 h (figure 9a). The results show that the growth rate for control,

pH 4 NPs, pH 5 NPs and pH 6 NPs was ca. 0.037, 0.034, 0.034 and 0.036 h^{-1}, respectively. It is indicated from the results that the highest growth rate was for control (without Au NPs) and the lowest and almost equal for pH 4 and 5 Au NPs (except antibiotic itself). Therefore, the Au NPs significantly affected the growth rate but it did not show satisfactory antibacterial activity in comparison to the CFD alone which is in consistent with the previous reports in the literature.[34,41,81] The reason behind these results was discussed in the previous section.

Reduction in cell survival

To assess the cell survival, the cells after overnight growth were washed, diluted in PBS buffer and incubated with Au NPs and antibiotics at a concentration ca. 64 µg/mL for a period of 24 h at 180 rpm, 37 ^{o}C. At 0 h and 24 h, the 100 µl aliquots were taken from each sample and plated on LB plates. The plates were incubated for 18 h to visualize the colony formation of cells and their digital photographs are shown in figure 9b. The colonies were counted and the histogram is shown in figure 9c. The results were surprising and did not match with the results from cell growth. It can be easily seen from the figure 9c that at 0 h, the colonies count were same for all the samples but after 24 h, the colony count was least for pH 4 sample which was followed by pH 6 and pH 5 NPs. On the other hand, the survival of bacterial cells was almost unaffected by antibiotic alone. It may be because the lactam antibiotics can only inhibit the cell growth by inhibiting the cell wall synthesis but cannot affect the cell survival. It was interesting to note that the Au NPs could reduce the cell survival but not the cell growth[82] which may be because the Au NPs could interact with the bacterial cells in PBS buffer, but could not in the LB medium.

Monitoring the changes in bacterial cell membrane upon interaction with Au NPs

In order to reveal the mechanism behind the damage to the bacterial cells by Au NPs (the result of cell survival), SEM study was carried out to examine the interaction between bacterial cells and Au NPs (figure 10). The bacterial cells were incubated with pH 4 Au NPs,

pH 5 Au NPs, pH 6 Au NPs and CFD for 4 h at a concentration ca. 64 μg/mL. The bacterial cells suspended in PBS buffer (without Au NPs incubation) were used as control and these cells did not show any damage in the SEM images. The similar type of killing pattern was found for all types of Au NPs and these results indicated that the irreversible damage (blabbing) to the cell walls probably occur by the direct contact of the Au NPs to the bacterial cells.[83,84] However, it can be observed from the figure 10 that the severity of damage was less in the case of antibiotic in comparison to Au NPs.

The fluorescence microscopic study has also been performed to monitor the changes in the cell membrane permeability using propidium iodide (PI) dye. The PI molecules can bind with DNA or RNA specifically to acquire enhanced fluorescence, but it cannot cross the membrane and is excluded from the viable cells. Intracellular staining of PI can identify dead cells.[85] It can be noticed from figure S19 that the cells got aggregated when incubated with pH 4 Au NPs and pH 5 Au NPs, in particular (as seen in DIC images in figures S19 c and e respectively). When the cells were treated with pH 4 Au NPs and pH 5 Au NPs, the diffused red fluorescent boundaries appeared around the cells (as visualized in the figures S19 d and f). This feature may be due to the combined effect of the damaged cell walls of the bacterial cells, which allowed the leakage of nucleic acid out of the cells and the aggregation of the cells.[86] These results are also consistent with the findings from SEM study. However, similar diffused red fluorescent boundaries in cells were not visible for the control cells (figure S19b) and CFD alone (figure S19j).

Oxidative stress by ROS production

Other than the cell wall damage mediated by the direct physical contact, a previous study on Au NPs cytotoxicity showed that the 'oxidative stress by ROS production' might also be one of the toxicity mechanisms.[87] The oxidative stress is also often suggested as a key mechanism behind the antibacterial properties of several other inorganic nanomaterials, such

as Ag NPs[88–91] and ZnO NPs.[92,93] We determined cellular ROS by using a DCF probe (originally non fluorescent), which can be easily oxidized to produce the fluorescent DCF by cellular ROS.[94] It can be observed from figure S20 that Au NPs did not induce an obvious increase of cellular ROS.

Conclusion

In summary, we have performed detailed experiments to understand the nucleation and growth of Au NPs and Au_8 QCs using cefradine molecule as both reducing and capping agent. This study has highlighted the important role of kinetics in the nanocrystals architecture. The $HAuCl_4$/CFD concentration, temperature and pH found to be very crucial factors in modulation of the Au NPs growth kinetics and hence, guiding the size and morphology of Au NPs. The growth of anisotropic Au NPs was shown to be significantly influenced by increase in the concentration, decrease in the temperature and decrease in the pH of the reaction. Experimental and theoretical studies show that oxygen, nitrogen and sulphur moieties are involved in the reduction and/or binding of CFD to Au NPs. The CV results show that the decrease in the reduction potential of CFD upon increase in the pH of the reaction from 4 to 6 leads to the growth of unstable Au NPs (ca. 20 nm) suspension to highly stable Au QCs (< 1 nm) suspension, respectively. MALDI-TOF result shows the synthesis of $[Au_8(CFD)_2S_6]$ QCs and their fluorescence was observed at ca. 432 nm with a Stokes shift of ca. 95 nm. Therefore, this study may be helpful in programmed and controlled nucleation and growth for synthesis anisotropic particles (unstable suspension) to quantum clusters (highly stable suspension).

Further, within a short reaction time, this strategy allows the fabrication of Au_8 QCs, having the capability to sense Hg^{2+} ions. On the basis of an aggregation-induced fluorescence quenching mechanism, these Au_8 QCs offer high selectivity and sensitivity with a limit of

detection of ca. 2 nM for the determination of Hg^{2+} ions. This Hg^{2+} ion sensing capability of the Au_8 QCs was also applied to directly detect the presence of 10 μM Hg^{2+} ions in the bacterial samples. We found that although antibiotic labeled Au NPs have negative surface charge, they show the decrease in *E. coli* cell growth rate. The least growth rate was found for pH 5 Au NPs. The antibiotic reduced Au NPs have also been shown to cause the significant reduction in the cell survival in comparison to antibiotic alone. The SEM results show that the antibacterial property of Au NPs is due to the degradation or blabbing of the cell walls of bacterial cells which was further confirmed by PI based fluorescence imaging of bacterial cells. The ROS assay shows that these Au NPs did not stimulate ROS production and hence, the possibility of ROS to be a mechanism behind loss of cell viability, was ruled out in our study. Our studies indicated that the most probable mechanism behind the damage in the bacterial cells is the direct contact to the bacterial cells by NPs.

Acknowledgement

PP acknowledges support from Young Scientist Award grant from Council for Scientific and Industrial Research (CSIR) in Physical Sciences and a separate grant from Department of Science & Technology (DST), India (DST/INT/ISR/P-8/2011). PP also acknowledges Dr. G. V. Pavan Kumar, Indian Institute of Science Education & Research (IISER), Pune, India for providing the facility of Raman spectrometer. PK, DKS and SS acknowledge the DBT for award of Junior Research Fellowship, CSIR for award of Nehru Post Doctorate Fellowship in Science and Senior Research Fellowship, respectively.

References

1 Z. Wu, J. Chen and R. Jin, *Adv. Funct. Mater.*, 2011, **21**, 177–183.

2 Z. Wu, M. A. Macdonald, J. Chen, P. Zhang and R. Jin, *J. Am. Chem. Soc.*, 2011, **133**, 9670–9673.

3 Z. Luo, V. Nachammai, B. Zhang, N. Yan, D. T. Leong, D. E. Jiang and J. Xie, *J. Am. Chem. Soc.*, 2014, **136**, 10577–10580.

4 E. E. Connor, J. Mwamuka, A. Gole, C. J. Murphy and M. D. Wyatt, *Small*, 2005, **1**, 325–327.

5 N. Li, P. Zhao and D. Astruc, *Angew. Chemie Int. Ed.*, 2014, **53**, 1756–1789.

6 H. K. Daima, P. R. Selvakannan, R. Shukla, S. K. Bhargava and V. Bansal, *PLoS One*, 2013, **8**, e796761–e7967614.

7 C. J. Murphy, A. M. Gole, J. W. Stone, P. N. Sisco, A. M. Alkilany, E. C. Goldsmith and S. C. Baxter, *Acc. Chem. Res.*, 2008, **41**, 1721–1730.

8 R. Jagannathan, P. Poddar and A. Prabhune, *J. Phys. Chem. C*, 2007, **111**, 6933–6938.

9 P. Khandelwal, D. K. Singh, S. Sadhu and P. Poddar, *Chempluschem*, 2014, **79**, 134–142.

10 R. Jagannathan, A. S. Parmar, S. Adyanthaya, A. Prabhune, M. Muschol and P. Poddar, *J. Phys. Chem. C*, 2009, **113**, 3478–3486.

11 H. Chen, L. Shao and J. Wang, *Chem. Soc. Rev.*, 2013.

12 T. A. Major, M. S. Devadas, S. S. Lo and G. V Hartland, *J. Phys. Chem. C*, 2013.

13 X. Huang, I. H. El-sayed and M. A. El-sayed, 2007, **2**, 681–693.

14 Y. Sun and Y. Xia, *Science*, 2002, **298**, 2176–2179.

15 O. R. Miranda, X. Li, L. Garcia-gonzalez, Z. Zhu, B. Yan, U. H. F. Bunz and V. M. Rotello, *J. Am. Chem. Soc.*, 2011, **133**, 9650–9653.

16 Y. Xiao, F. Patolsky, E. Katz, J. F. Hainfeld and I. Willner, *Science*, 2003, **299**, 1877–1881.

17 T. K. Sharma, R. Ramanathan, P. Weerathunge, M. Mohammadtaheri, H. K. Daima, R. Shukla and V. Bansal, *Chem. Commun.*, 2014, **50**, 15856–15859.

18 M. Stobiecka and M. Hepel, *Biomaterials*, 2011, **32**, 3312–3321.

19 H. Ding, D. Yang, C. Zhao, Z. Song, P. Liu, Y. Wang, Z. Chen and J. Shen, *ACS Appl. Mater. Interfaces*, 2015, **7**, 4713–4719.

20 G. E. Craig, S. D. Brown, D. a Lamprou, D. Graham and N. J. Wheate, *Inorg. Chem.*, 2012, **51**, 3490–3497.

21 B. Kang, M. M. Afifi, L. A. Austin, M. A. El-sayed, U. States, M. Science, O. Pathology and C. St, *ACS Nano*, 2013, **7**, 7420–7427.

22 Z. W. Wang and R. E. Palmer, *Nano Lett.*, 2012, **12**, 5510–5514.

23 P. Maity, S. Xie, M. Yamauchi and T. Tsukuda, *Nanoscale*, 2012, **4**, 4027–4037.

24 H. Häkkinen, *Chem. Soc. Rev.*, 2008, **37**, 1847.

25 J. Zheng, J. T. Petty and R. M. Dickson, *J. Am. Chem. Soc.*, 2003, **125**, 7780–7781.

26 S. Chen, R. S. Ingram, M. J. Hostetler, J. J. Pietron, R. W. Murray, T. G. Schaaff, J. T. Khoury, M. M. Alvarez and R. L. Whetten, *Science*, 1998, **280**, 2098–2101.

27 C. Félix, C. Sieber, W. Harbich and J. Buttet, *Phys. Rev. Lett.*, 2001, **86**, 2992–2995.

28 L. A. Peyser, A. E. Vinson, A. P. Bartko and R. M. Dickson, *Science*, 2001, **291**, 103–106.

29 J. Zheng, P. R. Nicovich and R. M. Dickson, *Annu. Rev. Phys. Chem.*, 2007, **58**, 409–431.

30 H. Yao, N. Kitaoka and A. Sasaki, *Nanoscale*, 2012, **4**, 955.

31 R. Fernandes, N. R. Smyth, O. L. Muskens, S. Nitti, A. Heuer-Jungemann, M. R. Ardern-Jones and A. G. Kanaras, *Small*, 2015, **11**, 713–721.

32 E. C. Cho, L. Au, Q. Zhang and Y. Xia, *Small*, 2010, **6**, 517–522.

33 P. Yan, R. Wang, N. Zhao, H. Zhao, D.-F. Chen and F.-J. Xu, *Nanoscale*, 2015, **7**, 5281–5291.

34 A. Rai, A. Prabhune and C. C. Perry, *J. Mater. Chem.*, 2010, **20**, 6789–6798.

35 M. H. Hyun, E. D. Jeong, M. S. Shin and J. S. Jin, *Bull. Korean Chem. Soc.*, 2008, **29**, 1185–1189.

36 O. A. Cephalosporins, *J Infect Dis.*, 1978, **137**, 490–493.

37 L. Shang, L. Yang, F. Stockmar, R. Popescu, V. Trouillet, M. Bruns, D. Gerthsen and G. U. Nienhaus, *Nanoscale*, 2012, **4**, 4155–4160.

38 G. L. Burygin, B. N. Khlebtsov, a N. Shantrokha, L. a Dykman, V. a Bogatyrev and N. G. Khlebtsov, *Nanoscale Res. Lett.*, 2009, **4**, 794–801.

39 Y. Zhao and X. Jiang, *Nanoscale*, 2013, **5**, 8340.

40 A. N. Brown, K. Smith, T. A. Samuels, S. O. Obare and M. E. Scott, *Appl. Environ. Microbiol.*, 2012, **78**, 2768–2774.

41 H. Gu, P. L. Ho, E. Tong, L. Wang and B. Xu, *Nano Lett.*, 2003, **3**, 1261–1263.

42 G. Chen, Z. Guo and L. Tang, *Analyst*, 2015, **140**, 5400–5443.

43 *Dynamics of Mercury Pollution on Regional and Global Scales: Atmospheric Processes and Human Exposures Around the World; Pirrone, N., Mahaffey, K. R., Eds.; Springer: New York, 2005.*, .

44 U. Kumar, A. Shete, A. S. Harle, O. Kasyutich, W. Schwarzacher, A. Pundle and P. Poddar, *Chem. Mater.*, 2008, **20**, 1484–1491.

45 B. Mazumder, I. Uddin, S. Khan, V. Ravi, K. Selvraj, P. Poddar and A. Ahmad, *J. Mater. Chem.*, 2007, **17**, 3910–3914.

46 I. Uddin, A. Jaiswal and P. Poddar, *Int. J. Innov. Biol. Res.*, 2013, **2**, 1–5.

47 C. Sharan, P. Khandelwal and P. Poddar, *RSC Adv.*, 2014, **5**, 1883–1889.

48 Y. Zhang, T. P. Shareena Dasari, H. Deng and H. Yu, *J. Environ. Sci. Heal. Part C*, 2015, **33**, 286–327.

49 A. Sengupta and P. Hazra, *Chem. Phys. Lett.*, 2010, **501**, 33–38.

50 M. J. Frisch, G. W. Trucks, H. B. Schlegel and G. E. Scuseria et al., *Off. Gaussian 09 Lit. Cit. Gaussian, Inc., Wallingford CT Gaussian 09.*

51 D. K. Singh, S. K. Srivastava and B. P. Asthana, *Chem. Phys.*, 2011, **380**, 24–33.

52 D. K. Singh, S. K. Srivastava, S. Schlücker, R. K. Singh and B. P. Asthana, *J. Raman Spectrosc.*, 2011, **42**, 851–858.

53 S. Singh, D. K. Singh, S. K. Srivastava and B. P. Asthana, *Vib. Spectrosc.*, 2011, **56**, 26–33.

54 D. K. Singh and B. P. Asthana, *J Mol Model*, 2012, **18**, 3541–3552.

55 P. J. Hay and W. R. Wadt, *J. Chem. Phys.*, 1985, **82**, 299–310.

56 D. K. Singh, E. O. Ganbold, E. M. Cho, K. H. Cho, D. Kim, J. Choo, S. Kim, C. M. Lee, S. I. Yang and S. W. Joo, *J. Hazard. Mater.*, 2014, **265**, 89–95.

57 A. T. N. Lam, J. Yoon, E.-O. Ganbold, D. K. Singh, D. Kim, K.-H. Cho, S. Y. Lee, J. Choo, K. Lee and S.-W. Joo, *Colloids Surfaces B Biointerfaces*, 2014, **123**, 61–67.

58 A. T. N. Lam, J. Yoon, E.-O. Ganbold, D. K. Singh, D. Kim, K.-H. Cho, S. J. Son, J. Choo, S. Y. Lee, S. Kim and S.-W. Joo, *J. Colloid Interface Sci.*, 2014, **425**, 96–101.

59 B. Mennucci and J. Tomasi, *J. Chem. Phys.*, 1997, **106**, 5151–5158.

60 A. Rai, A. Singh, A. Ahmad and M. Sastry, *Langmuir*, 2006, **22**, 736–741.

61 S. S. Shankar, S. Bhargava and M. Sastry, *J. Nanosci. Nanotech.*, 2005, **5**, 1721–1727.

62 Yuen-sheng Chiang and John Turkevich, *J. Colloid Sci.*, 1963, **18**, 772–783.

63 J. A. A. Engelbrecht and H. C. Snyman, *Gold Bull.*, 1983, **16**, 1–4.

64 R. Shukla, V. Bansal, M. Chaudhary, A. Basu, R. R. Bhonde and M. Sastry, *Langmuir*, 2005, **21**, 10644–10654.

65 B. Tzeng and S. Peng, *J. Chem. Soc., Dalt. Trans.*, 1996, 1769–1770.

66 S. Shieh, D. Li and S. Peng, *J. Chem. Soc., Dalt. Trans.*, 1993, 195–196.

67 *Sargent-Welch Table Period. Prop. Elem. Sargent-Welch Sci. Company, Skokie, 1980.*, 1980.

68 B. Höffling, F. Ortmann, K. Hannewald and F. Bechstedt, *Phys. Rev. B - Condens. Matter Mater. Phys.*, 2010, **81**, 1–12.

69 E. M. Cho, D. K. Singh, E. O. Ganbold, U. Dembereldorj, S. W. Jang, D. Kim, J. Choo, S. Kim, C. M. Lee, S. I. Yang and S. W. Joo, *Appl. Spectrosc.*, 2014, **68**, 307–314.

70 D. K. Singh, R. Jagannathan, P. Khandelwal, P. M. Abraham and P. Poddar, *Nanoscale*, 2013, **5**, 1882–1893.

71 D. K. Singh, E.-O. Ganbold, E.-M. Cho, C. M. Lee, S. I. Yang and S.-W. Joo, *J. Mol. Struct.*, 2013, **1049**, 464–472.

72 J. Zheng, C. Zhang and R. Dickson, *Phys. Rev. Lett.*, 2004, **93**, 0774021–0774024.

73 H. Kawasaki, K. Hamaguchi, I. Osaka and R. Arakawa, *Adv. Funct. Mater.*, 2011, **21**, 3508–3515.

74 X. Le Gu, H. Benjamin, G. Jung, K. Hollemeyer, V. Trouillet and M. Schneider, *J. Phys. Chem. C*, 2011, **115**, 10955–10963.

75 T.-H. Chen and W.-L. Tseng, *Small*, 2012, **8**, 1–8.

76 M. A. Habeeb Muhammed, S. Ramesh, S. S. Sinha, S. K. Pal and T. Pradeep, *Nano Res.*, 2008, **1**, 333–340.

77 P. L. Xavier, K. Chaudhari, P. K. Verma, S. K. Pal and T. Pradeep, *Nanoscale*, 2010, **2**, 2769–2776.

78 W. Guo, J. Yuan and E. Wang, *Chem. Commun.*, 2012, **48**, 3076–3078.

79 X. Yang, Y. Su, M. C. Paau and M. M. F. Choi, *Anal. Chem.*, 2012, **84**, 1765–1771.

80 Z. V. Feng, I. L. Gunsolus, T. a. Qiu, K. R. Hurley, L. H. Nyberg, H. Frew, K. P. Johnson, A. M. Vartanian, L. M. Jacob, S. E. Lohse, M. D. Torelli, R. J. Hamers, C. J. Murphy and C. L. Haynes, *Chem. Sci.*, 2015, **6**, 5186–5196.

81 M. Demurtas and C. C. Perry, *Gold Bull.*, 2014, **47**, 103–107.

82 M. R. Smith, M. G. Boenzli, V. Hindagolla, J. Ding, J. M. Miller, J. E. Hutchison, J. a Greenwood, H. Abeliovich and A. T. Bakalinsky, *Appl. Environ. Microbiol.*, 2013, **79**, 728–733.

83 A. Fonseca, S. Nejati, M. Elimelech, E. Engineering, N. Haven and U. States, *ACS Nano*, 2015, **9**, 7226–7236.

84 A. Regiel-Futyra, M. Kus-Liśkiewicz, V. Sebastian, S. Irusta, M. Arruebo, G. Stochel and A. Kyzioł, *ACS Appl. Mater. Interfaces*, 2015, **7**, 1087–1099.

85 Y. Zhao, Y. Tian, Y. Cui, W. Liu, W. Ma and X. Jiang, *J. Am. Chem. Soc.*, 2010, **132**, 12349–12356.

86 Y. Zhao, Y. Tian, Y. Cui, W. Liu, W. Ma and X. Jiang, *J. Am. Chem. Soc.*, 2010, **132**, 12349–12356.

87 Y. Pan, A. Leifert, D. Ruau, S. Neuss, J. Bornemann, G. Schmid, W. Brandau, U. Simon and W. Jahnen-Dechent, *Small*, 2009, **5**, 2067–2076.

88 S. Kim, J. E. Choi, J. Choi, K.-H. Chung, K. Park, J. Yi and D.-Y. Ryu, *Toxicol. Vitr.*, 2009, **23**, 1076–1084.

89 S. Kim and D.-Y. Ryu, *J. Appl. Toxicol.*, 2013, **33**, 78–89.

90 J. Eun, S. Kim, J. Hee, P. Youn, J. Seok, K. Park, J. Yi and D. Ryu, *Aquat. Toxicol.*, 2010, **100**, 151–159.

91 W. Zhang, Y. Li, J. Niu and Y. Chen, *Langmuir*, 2013, **29**, 4647–4651.

92 V. Sharma, D. Anderson and A. Dhawan, *Apoptosis*, 2012, **17**, 852–870.

93 J. Wang, X. Deng, F. Zhang, D. Chen and W. Ding, *Nanoscale Res. Lett.*, 2014, **9**, 1–12.

94 Y. Cui, Y. Zhao, Y. Tian, W. Zhang, X. Lü and X. Jiang, *Biomaterials*, 2012, **33**, 2327–2333.

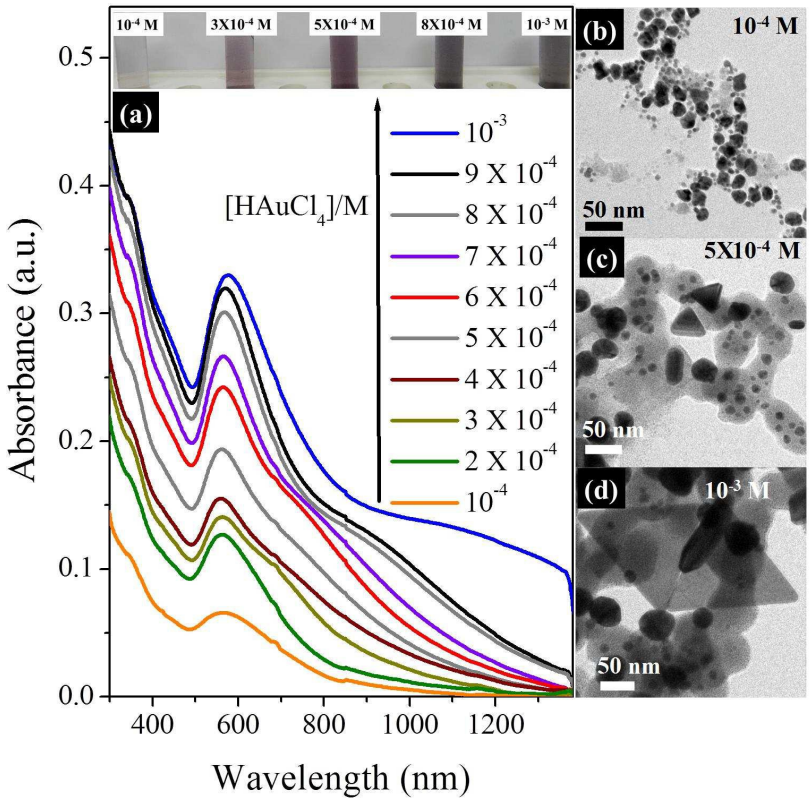

Figure 1. (a) The UV-vis-NIR spectra for the CFD labeled Au NPs synthesized at various final concentrations of $HAuCl_4$ (10^{-4} M to 10^{-3} M) while keeping the CFD final concentration same to 5×10^{-4} M. The absorbance values for various curves are shifted with respect to each other for the sake of clarity. Particles synthesized at larger concentration of $HAuCl_4$ show increasing absorption at near-infrared due to increasing proportion of anisotropic nanostructures. TEM images of CFD labeled Au NPs synthesized at various final concentrations of $HAuCl_4$ (b) 10^{-4} M, (c) 5×10^{-4} M, and (d) 10^{-3} M while keeping the CFD final concentration same to 5×10^{-4} M. The polydispersity of the nanoparticles is due to inherently slow reaction kinetics as the antibiotic molecules are considered weak reducing agents. The co-existence of smaller particles can also be noticed. The TEM images also show formation of increasing proportion of anisotropic structures (hexagons, triangles) in comparison to quasi-spherical structures for higher concentration of $HAuCl_4$.

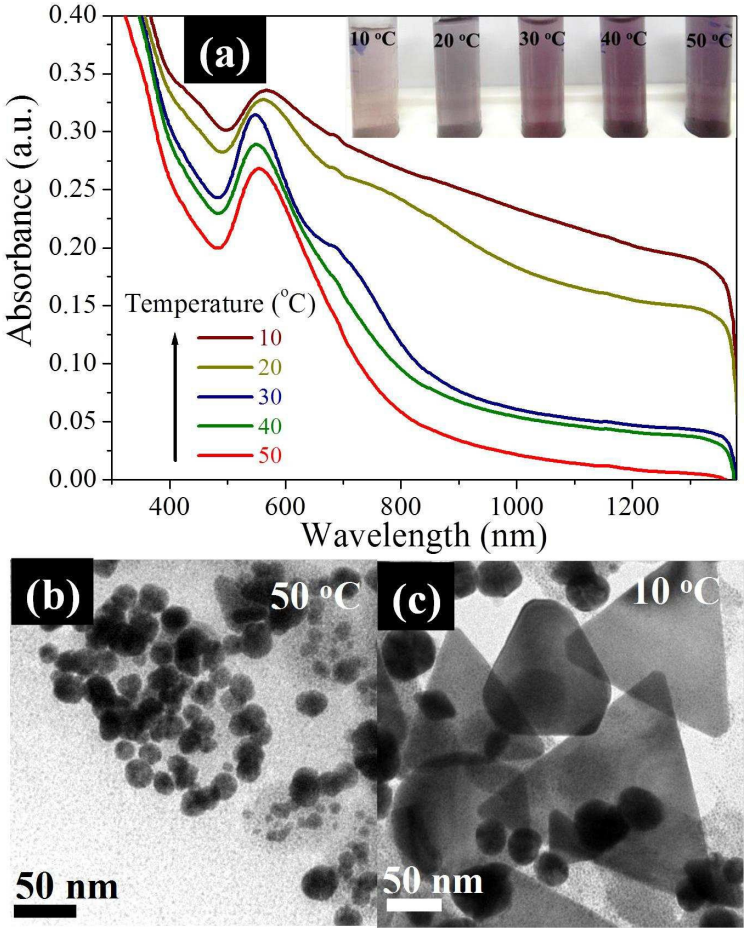

Figure 2. (a) UV-vis-NIR spectra of CFD labeled Au NPs synthesized at various temperatures (at final concentration of 5×10^{-4} M for both $HAuCl_4$ and CFD). The absorbance values for various curves are shifted with respect to each other for the sake of clarity. These results conclude the formation of isotropic structures at higher temperature due to increased growth in contrast to anisotropic structures at lower temperatures. TEM images of CFD labeled Au NPs synthesized at (b) 50 °C, and (c) 10 °C of reaction temperature when the final concentration of both CFD and $HAuCl_4$ was 5×10^{-4} M. These images clearly show the formation quasi-spherical particles at higher temperatures and a fraction of anisotropic particles at lower temperatures.

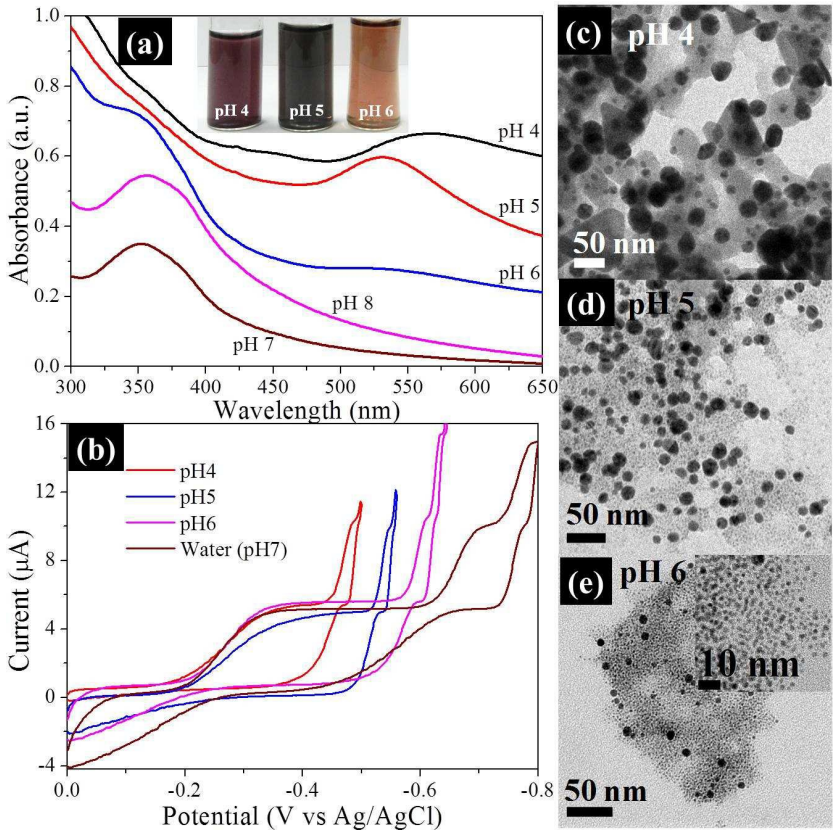

Figure 3. (a) UV-vis-NIR spectra of CFD labeled Au NPs synthesized at various pH values. Inset shows the color change at different pH values (at final concentration of 5×10^{-4} M for both $HAuCl_4$ and CFD). The absorbance values for various curves are shifted with respect to each other for the sake of clarity. (b) Cyclic voltammetry curves of antibiotic (CFD) in different pH environments showing the shift in reduction potential according to the pH of the environment. TEM images of CFD labeled Au NPs synthesized at (c) pH 4, (d) pH 5 and (e) pH 6 when final concentration of both CFD and $HAuCl_4$ was 5×10^{-4} M. The comparison shows synthesis of smaller nanoparticles at higher pH values.

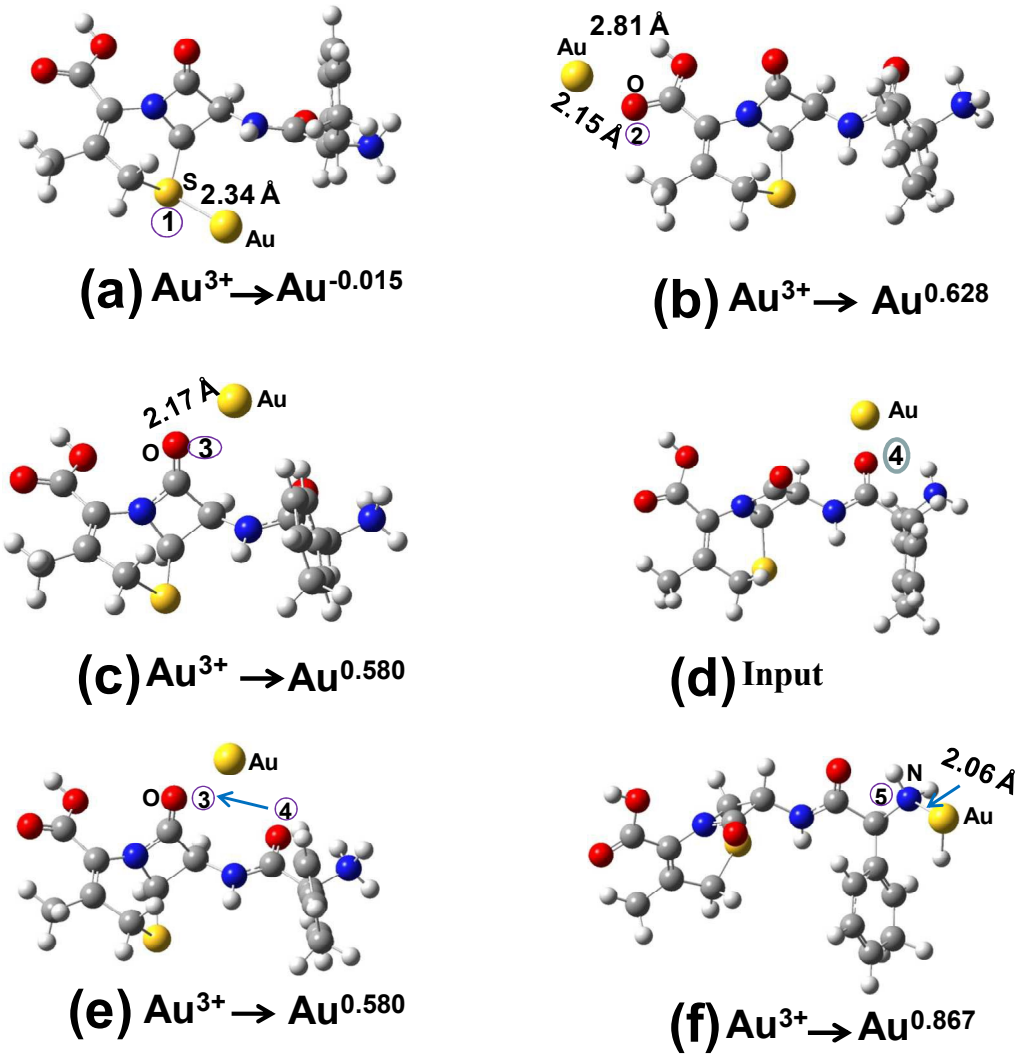

Figure 4. Optimized interactions of CFD monomers with single Au^{3+} ion in aqueous environment using PCM approach (a) CFD + 1 Au_1, (b) CFD + 1 Au_2, (c) CFD + 1 Au_3, (d) input geometry of CFD + 1 Au_4, (e) output geometry of CFD + 1 Au_4 (f) CFD + 1 Au_5. [Gray, white, red, blue and yellow colors indicate the carbon, hydrogen, oxygen, nitrogen, and sulfur atoms, respectively. However, Au^{3+} is mentioned in different figures separately].

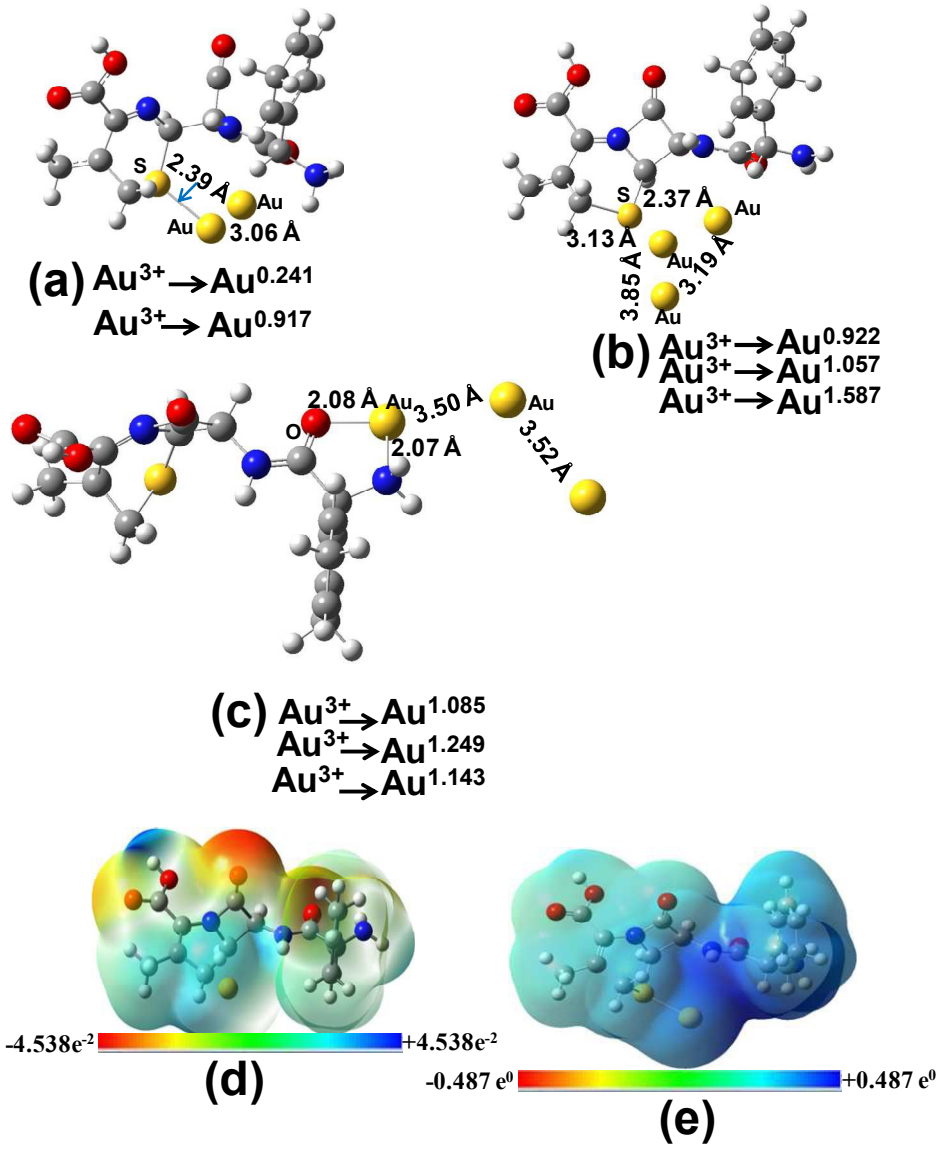

Figure 5. Optimized interactions of CFD with two and three Au^{3+} ions in aqueous environment using PCM approach (a) CFD + 2 Au_1, (b) CFD + 3 Au_1, (c) CFD + 3 Au_5. Electron density from total SCF density (isoval=0.0004; {mapped with electrostatic potential from total SCF density}) (d) CFD, (e) CFD + 1 Au_1. [The colors of the atoms are discussed in figure 4].

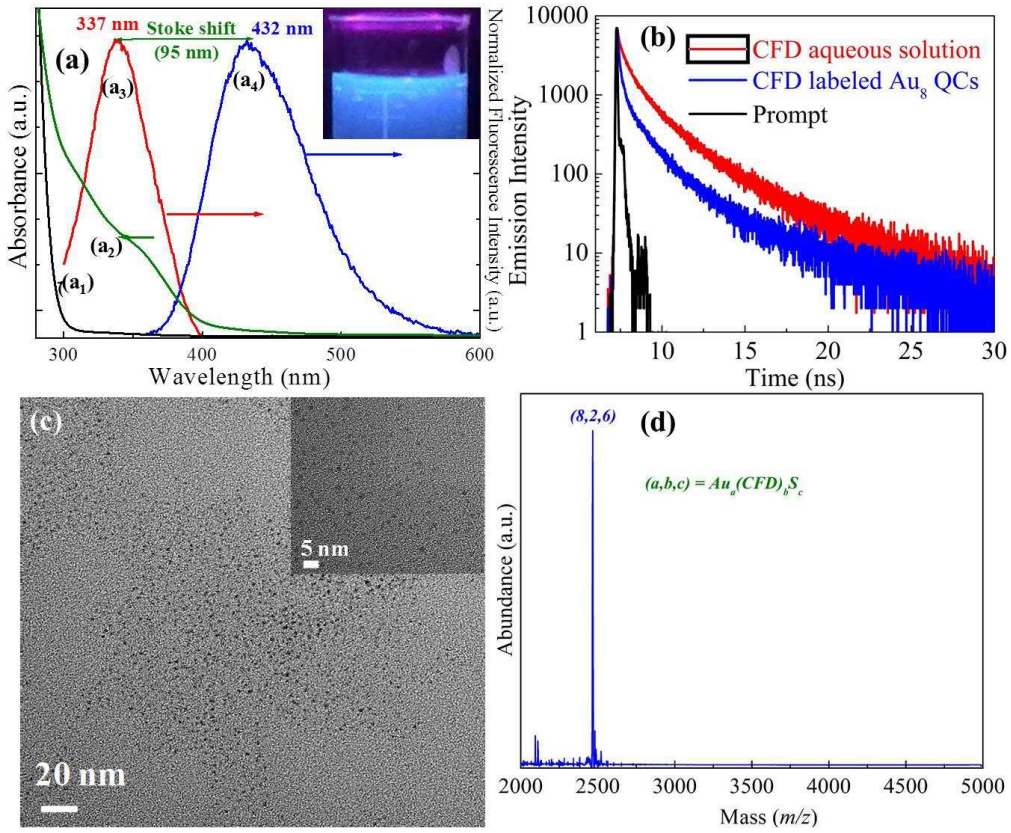

Figure 6. (a) Absorbance spectra of (a_1) CFD aqueous solution and (a_2) CFD labeled Au QCs; fluorescence (a_3) excitation spectrum and (a_4) emission spectrum of CFD labeled Au QCs. Inset shows blue emissive CFD labeled Au QCs suspension which confirms the formation of quantum clusters. (b) Fluorescence decay of the CFD aqueous solution and Au_8 QCs collected at ca. 432 nm (excited at 337 nm). (c) HR-TEM image of CFD labeled Au_8 QCs and its magnified view (inset). (d) Positive ion linear mode MALDI-TOF mass spectrum for CFD labeled Au_8 QCs. The mass spectrum was baseline corrected by using the Data Explorer software.

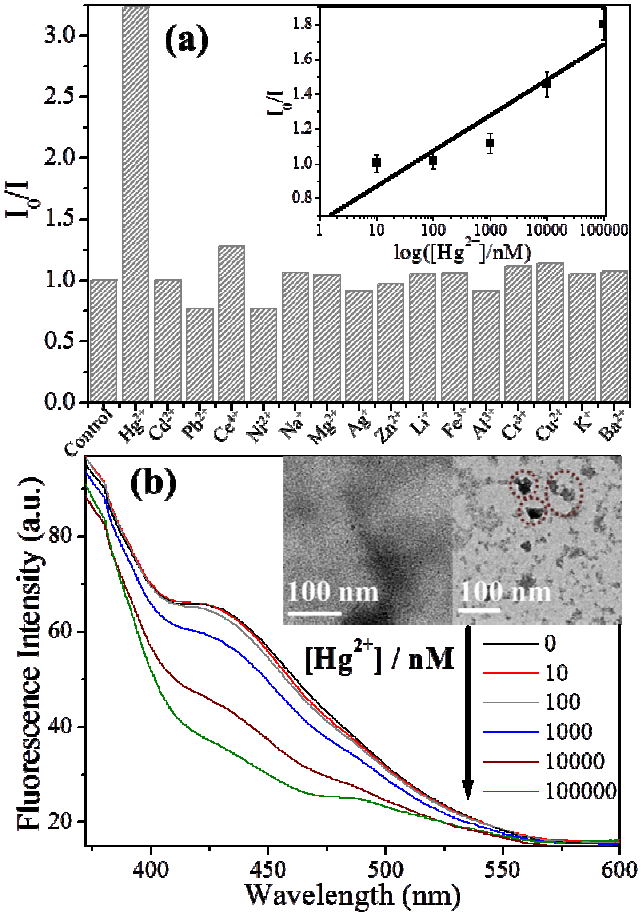

Figure 7. (a) Relative fluorescence (I_0/I) of CFD labeled Au_8 QCs at an excitation wavelength ca. 337 nm in the presence of various metal ions (Hg^{2+}, Cd^{2+}, Pb^{2+}, Ce^{4+}, Ni^{2+}, Cr^{3+}, Ag^{+}, Li^{+}, Mg^{2+}, Al^{3+}, K^{+}, Ba^{2+}, Zn^{2+}, Cu^{2+}, Na^{+} and Fe^{3+}). The concentration of all the metal ions was 100 μM; I_0 and I correspond to the fluorescence intensity of Au_8 QCs in the absence and presence of metal ions, respectively. Inset shows the sensitivity plot between relative fluorescence intensity (I_0/I) value and the log value of Hg^{2+} ions concentration. (b) Fluorescence spectra of CFD labeled Au_8 QCs at an excitation wavelength ca. 337 nm in the presence of increasing concentration of Hg^{2+} ions. The black arrow shows that fluorescence decreases upon increase in the concentration of Hg^{2+} ions (0, 10, 100, 1000, 10000, 100000 nM. Inset shows the TEM images of CFD labeled Au_8 QCs before and after treatment with Hg^{2+} ions. Red circles show the aggregation of Au_8 QCs upon interaction with Hg^{2+} ions.

Table 1. Time resolved fluorescence decay study of CFD aqueous solution and CFD labeled Au_8 QCs.

Sample	$\bar{N}_1$	$\bar{N}_2$	$\bar{N}_3$	τ_1 (ns)	τ_2 (ns)	τ_3 (ns)	$\langle\tau\rangle$ (ns)	χ^2
CFD aqueous solution	0.028	0.071	0.007	0.94	3.44	0.12	2.56	1.08
CFD labeled Au_8 QCs	0.009	0.001	0.124	1.21	4.82	0.097	0.2	1.07

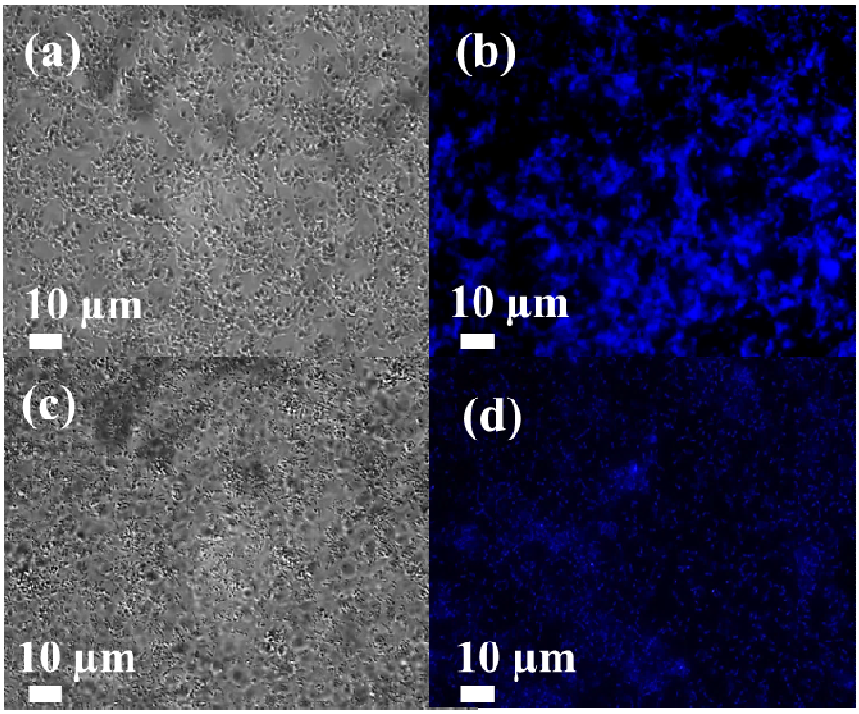

Figure 8. The DIC images (a, c) and the fluorescence microscopic images (b, d) of bacterial cells incubated with blue luminescent Au_8 QCs for 2 h in absence of mercury ions (a, b) and in presence of 10 μM mercury ions (c, d).

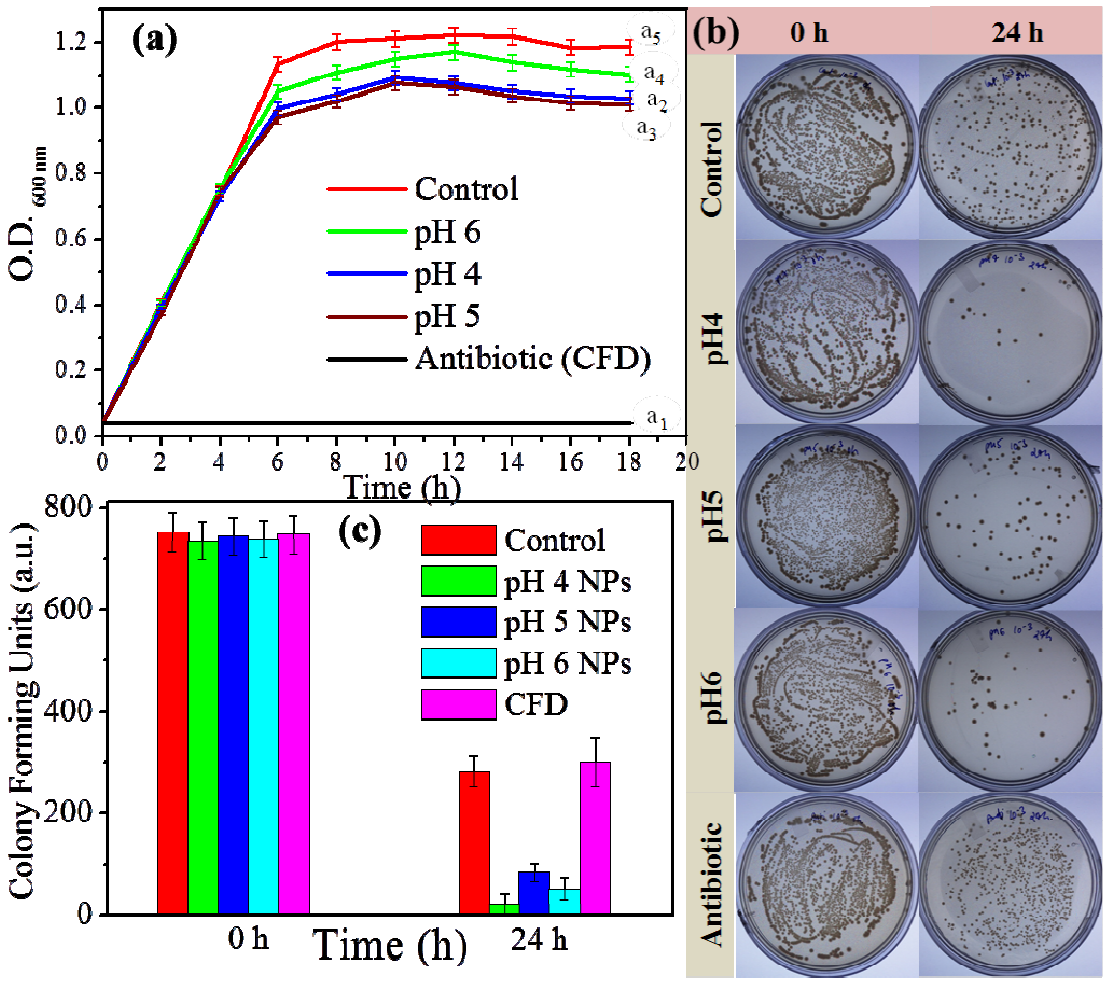

Figure 9. (a) Growth curves of *E. coli* cells exposed to (a_1) CFD antibiotic, (a_2) pH 4 Au NPs, (a_3) pH 5 Au NPs, (a_4) pH 6 Au NPs, and (a_5) without Au NPs at a concentration of 64 μg/mL. All data are the mean ± standard deviation of triplicate determinations. (b) Cell survival assay performed using LB agar petri-dishes inoculated with *E. coli*, showing the almost same number of colonies at 0 h (in the first row) and decreased number of colonies after 24 h (in second row) upon incubation with different size and shape of Au NPs synthesized at different pH conditions (pH 4, pH 5, and pH 6). It should be noted that Au NPs were dialyzed for 24 h with two times water change to negate the contribution from different pH buffers and precursors. (c) Histogram showing the cell survival before and after 24 h of exposure of antibiotic (CFD) and Au NPs synthesized at pH 4, pH 5, and pH 6.

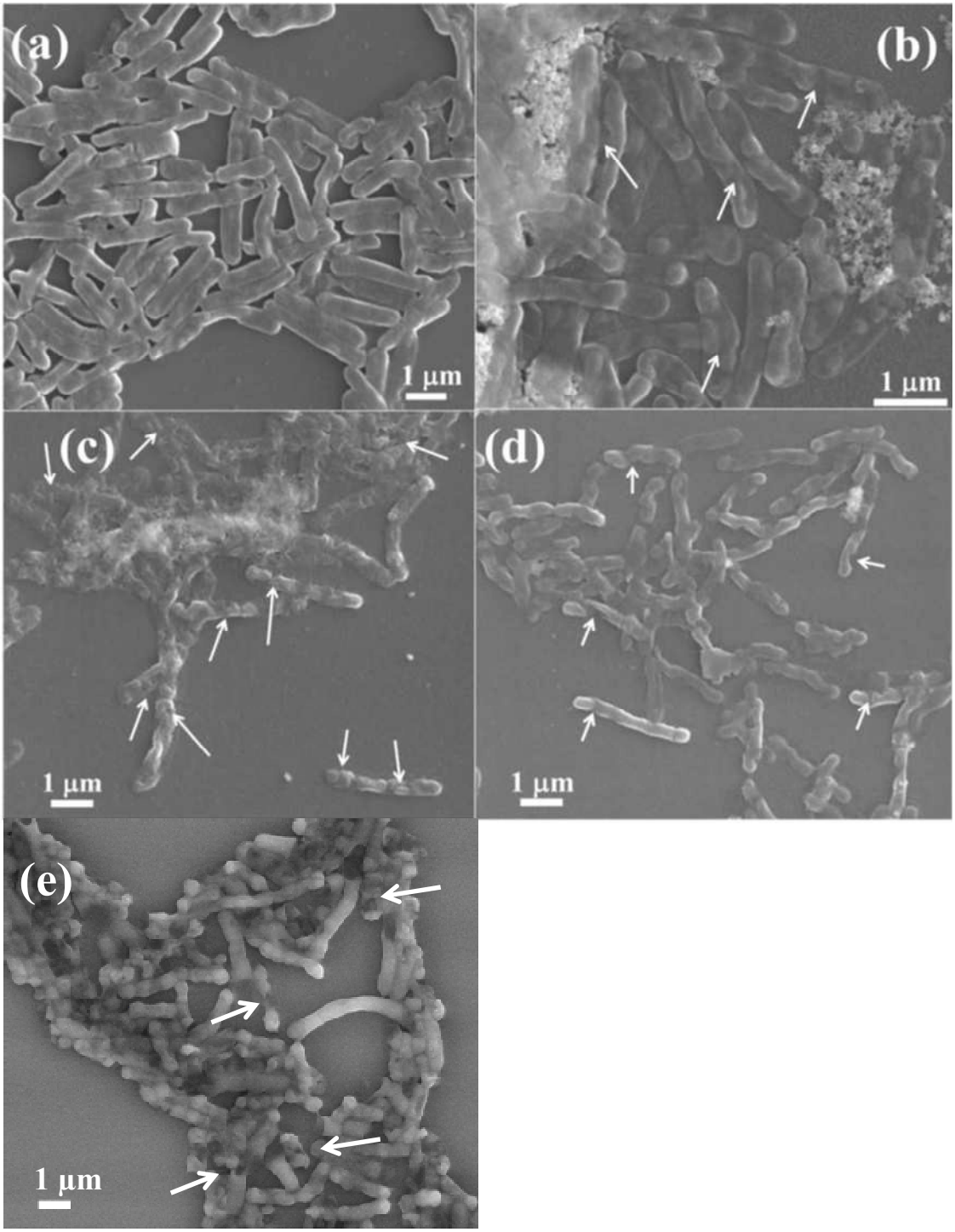

Figure 10. SEM images of *E. coli* cells incubated with (a) saline solution, (b) pH 4 Au NPs, (c) pH 5 Au NPs, and (d) pH 6 Au NPs (e) antibiotic (CFD) at a concentration of 64 μg/mL for 4 h. White arrows indicate the degraded cell walls of bacterial cells.